Coastal Engineering 114 (2016) 99–118

Contents lists available at ScienceDirect

Coastal Engineering

journal homepage: www.elsevier.com/locate/coastaleng

Two-way coupled long wave - RANS model: Solitary wave transformation and breaking on a plane beach

William J. Pringle [a,*], Nozomu Yoneyama [b], Nobuhito Mori [b]

[a] Department of Urban Management, Graduate School of Engineering, Kyoto University, Kyoto daigaku-Katsura, Nishikyo-ku, Kyoto 615-8530, Japan
[b] Disaster Prevention Research Institute, Kyoto University, Uji Campus, Gokasho, Uji 611-0011, Japan

ARTICLE INFO

Article history:
Received 11 June 2015
Received in revised form 6 February 2016
Accepted 2 April 2016
Available online 3 May 2016

Keywords:
Two-way coupling
Shallow water equations
RANS
Shoaling
Solitary waves
Wave breaking

ABSTRACT

A two-way coupled long wave to Reynolds-averaged Navier–Stokes (RANS) wave model named 2CLOWNS is introduced in this study and its numerical procedure is described in detail. The model is applied to solitary wave transformation and breaking on plane beaches with slopes 1/100, 1/60, 1/35 and 1/20. Two-way coupling was verified for test cases of pure solitary wave reflection on a flat bed, and wave transformation on slopes including rundown. The algorithm becomes sufficiently robust when a no gradient boundary condition on the vertical velocities is applied, the local wave height and slope are sufficiently small, and the coupling depths are sufficiently large. Suggested limits to the local wave height and slope are outlined. Characteristics of shoaling prior to breaking are analysed in detail for the long wave model. Optimal depths for coupling to the RANS model are found that approximately correspond to the transition from gradual shoaling to rapid shoaling. An expression that estimates this location is presented based on a nondimensional slope parameter. Overall, 2CLOWNS is shown to approximate shoaling and breaking characteristics in comparison with theory, physical experiments and other numerical analyses. The post-breaking behaviour and wave shape approximate theoretical descriptions and experimental observations including the touchdown of the plunging jet and resulting splashup. Velocity profiles are shown to be considerably different to ones based on depth-integrated models just prior to wave breaking and thereafter. 2CLOWNS allows for more reliable simulations when computing wave propagation from far offshore towards the coast in reduced computational time compared with full RANS simulations under the appropriate conditions outlined in this study.

1. Introduction

In long wave modelling it is important to obtain good estimations of wave shoaling and breaking in the nearshore area. These phenomena can affect sediment transport, hydrodynamic forces on coastal structures and transport of driftage significant during tsunami and storm disasters. As a representation of tsunamis and other long waves a significant amount of attention has been paid to the evolution of solitary waves. (Synolakis, 1987) derived an analytical solution to the nonlinear shallow water equations valid for non-breaking solitary waves. These solutions have been often used in tsunami benchmarking (Synolakis et al., 2009). Concerning breaking waves where dispersion and nonlinearity become important hence the (Synolakis, 1987) solutions out of range, (Synolakis and Skjelbreia, 1993) provided a semi-quantitative description of their evolution. Four distinct regions of solitary wave transformation were identified where the rate of shoaling could be approximated according to a power law equivalent to Green's law and Boussinesq's law in the gradual and rapid shoaling stages respectively, followed by rapid and gradual decay after wave breaking. Both (Hsiao et al., 2008; Hwang et al., 2007) presented experimental studies investigating breaking solitary waves on a mild 1/60 slope. (Hsiao et al., 2008) confirmed the analysis of (Synolakis and Skjelbreia, 1993) and further identified a fifth region corresponding to post-breaking bore propagation. (Grilli et al., 1994; Grilli et al., 1997) developed a fully nonlinear potential flow (FNPF) model that was applied to the transformation of solitary waves on plane slopes and was shown to be in excellent agreement with experiments performed on a 1/35 slope. They proposed empirical formulae for breaking characteristics based on a nondimensional slope parameter. (Hsiao et al., 2008) also shows that their formulae were in good agreement on the mild slope. However, (Grilli et al., 1994; Grilli et al., 1997) note that on the steeper slopes (>1/35) Green's law and Boussinesq's law are not very good descriptors of solitary wave evolution and in fact on very steep slopes the solitary wave height essentially does not change in height at all.

To model solitary waves and other long waves from far offshore to onshore, depth-averaged/integrated two dimensional wave equations (2DH) have been typically utilized, in particular the shallow water

* Corresponding author.
E-mail addresses: wjpringlevii@gmail.com (W.J. Pringle), yoneyama.nozomu.4w@kyoto-u.ac.jp (N. Yoneyama), mori@oceanwave.jp (N. Mori).

http://dx.doi.org/10.1016/j.coastaleng.2016.04.011

equations (NSWE) for tsunami modelling. (Titov and Synolakis, 1995) presented an alternating direction implicit (ADI) approach by splitting the 2DH NSWE into two single-dimensional formulations allowing for one-dimensional (1DH) consideration of the inundation algorithm. Furthermore, numerical models such as TUNAMI (Imamura et al., 2006) and COMCOT (Liu et al., 1998) have been commonly applied with reasonable success and are well adapted to computing over large scales with various spatial resolutions (grid nesting). When linear dispersive effects are important for long distance propagation, numerical dispersion inherent in the model can be utilized in TUNAMI and COMCOT to match those of the linear Boussinesq equations (Cho et al., 2007). However, for more local dispersive effects Boussinesq models are better suited. Both weakly nonlinear (Wei and Kirby, 1995; Nwogu, 1993; Madsen and Sorensen, 1992) and fully nonlinear Boussinesq models (FNBM) (e.g. COULWAVE (Kim et al., 2009) and FUNWAVE (Shi et al., 2012)) exist, the latter showing excellent performance for shoaling on slopes over a wide range of nonlinearity ratios (Wei et al., 1995). COULWAVE is also formally 'weakly-rotational', a rare divergence from the typical irrotational assumption of most long wave models that otherwise have ad hoc or no consideration of mixing effects aside from numerical manifestations.

Depth-integrated models are not exact forms of the governing equations of fluid motion and contain theoretically a truncation error of some order (Wei et al., 1995). They also lose the ability to model wave-overturning and other three-dimensional effects. However, some models have been developed to solve the original fully nonlinear potential flow (FNPF) equations, in particular a boundary element method (BEM) (Grilli et al., 1994; Grilli et al., 1997). Such models however breakdown on the touchdown of the overturning jet before turbulent effects become significant. To simulate the physics hereafter and provide detailed information on turbulence and bottom stresses as well as interaction with irregularly shaped structures Navier–Stokes (NS) based solvers are required. Such solvers however suffer from very high computational costs, require a fine resolution in space and time to model the physics of the problem to greater accuracy than its depth-integrated counterpart, and are often susceptible to numerical dissipation over long distances due to the indirect modelling of the free surface and thus are not suitable for calculation over wide areas.

Typically though the advantages of NS models may only encompass a relatively small area around a structure or region of interest particularly around the time when wave breaking would occur. This realization has encouraged modellers to investigate coupling between depth-integrated long wave models and NS models in space to obtain the advantages and reduce the disadvantages of both models. Most NS models adopted are traditionally of the Reynolds-averaged type (RANS) that are computationally efficient in comparison to direct numerical simulation (DNS) and Large eddy Simulation (LES) types. (Fujima et al., 2002; Fujima, 2006) first demonstrated this type of hybrid model using the NSWE combined with a single free surface RANS model. (Sitanggang and Lynett, 2010) presented and validated a scheme that couples a FNBM (COULWAVE) model and a vertical two-dimensional (2DV) RANS model. Further, (Pringle and Yoneyama, 2013) applied a coupled model using the NSWE with a fully three-dimensional RANS model to the 2011 Tohoku Tsunami in Kamaishi Bay, Iwate Prefecture with reasonable success. However, little comprehensive research on the validation of coupling depth-integrated long wave equations with RANS models has been conducted. Moreover, it is required to evaluate errors when matching the solutions of the two models at the interface and optimise locations of that interface.

In this study a fully developed version of the two-way coupled long wave to RANS model based on (Pringle and Yoneyama, 2013) is described in detail considering two-way coupling in 1DH and 2DV. The coupled model will hereafter be referred to as 2CLOWNS (**2**-way **C**oupled **Lo**ng **W**ave to **N**avier–**S**tokes model). To evaluate the capabilities of 2CLOWNS and its constituent models, solitary wave shoaling and breaking characteristics on a plane beach are analysed in detail for a range of slopes and offshore wave heights. Wave transformation in the individual long wave (NSWE), RANS, and FNBM (COULWAVE) models is compared. Regions where differences become significant in the NSWE model are identified to determine optimal coupling positions to the RANS model in 2CLOWNS. The two-way coupling algorithm is verified with tests that include reflection of waves against a vertical wall and a steep slope. Sensitivity to the velocity boundary conditions to the RANS model, coupling depths, and experimental conditions are summarised. Prediction of the wave breaking characteristics such as the water depth at breaking and the breaker index by 2CLOWNS are compared with experiments and the FNPF model. Furthermore, the post-breaking wave behaviour and wave shape in 2CLOWNS is compared qualitatively with physical experimental observations to demonstrate its ability to model the entire wave transformation and breaking process. Finally, velocity profiles of 2CLOWNS and depth-integrated models are shown for comparison, and their disparities are discussed.

2. Long wave equation model

2.1. Governing equations

Depth-averaged shallow water equations (NSWE) provide a strong backbone to long wave modelling because of their hyperbolic nature. Even state-of-the-art depth-integrated Boussinesq models reduce to the NSWE if dispersion terms are ignored, a convenience when considering wave breaking problems in order to add numerical dissipation into models through shock-capturing techniques (Roeber and Cheung, 2012). NSWE in their own right are powerful tools for tsunami simulation and in most cases are perfectly acceptable for modelling propagation through to inundation (Shuto, 1991). The NSWE in conservative form with additional bottom friction and linear dispersion effects in one-dimension are:

$$\frac{\partial \eta}{\partial t}+\frac{\partial Q}{\partial x}=0 \tag{1}$$

$$\frac{\partial Q}{\partial t}+\frac{\partial}{\partial x}\left(\frac{Q^2}{H}\right)+gH\frac{\partial \eta}{\partial x}+\frac{gn^2Q^2}{H^{7/3}}=h\frac{\partial \psi}{\partial x} \tag{2}$$

where η is the surface elevation, h is the still water depth, $H=h+\eta$ is the total water depth, Q is the volume flux, g is the acceleration due to gravity, n is Manning's friction coefficient, and ψ is the dispersion potential function defined as:

$$\psi=\left(\gamma+\frac{1}{3}\right)h\frac{\partial^2 Q}{\partial x\partial t}+\gamma g h^2\frac{\partial^2 \eta}{\partial x^2} \tag{3}$$

Following (Shigihara and Fujima, 2007), $\gamma=1/15$ corresponds to linear dispersion characteristics valid up to offshore length ratios (defined in §5.1), $h_0/L_0=0.5$ (Madsen et al., 1991) which is more than adequate for this study and is thus adopted.

2.2. Numerical scheme

The numerical scheme employed is the explicit staggered leap-frog method for solving the set of Eqs. (1) and (2) sans the dispersion term, i.e. with the RHS of Eq. (2) equal to zero. When linear frequency dispersion is included an additional implicit correction step as proposed by (Shigihara and Fujima, 2007) is adopted. The linear components of the scheme are solved using second-order staggered central differences, and the nonlinear advection terms are solved using first-order upwind differencing. The difference formulations including the implicit correction step are detailed in Appendix A, and the stencil is shown in Fig. 1. The resulting solution is stable and robust but the low-order differencing means the scheme is susceptible to numerical diffusion and dissipation (Son et al., 2011). Nevertheless, the scheme is fast, efficient and grid

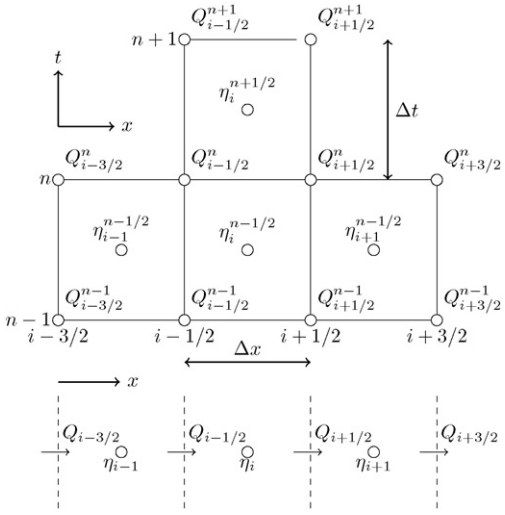

Fig. 1. Finite difference stencil in time and space for the staggered leapfrog method.

nesting is easily formulated and achieved. Thus, the leapfrog scheme is well suited for large scale geophysical simulations e.g. tsunami simulations from source to inundation. Through TUNAMI, COMCOT and other model variations the scheme is commonly adopted by researchers and government agencies alike.

In addition, a key modification as detailed in Appendix A is made to improve both the accuracy and stability of the nonlinear advection terms when considering the implicit correction step for linear frequency dispersion. As mentioned above the first-order upwind differencing of the nonlinear terms adds significant numerical diffusion to the model. However, the leading-order truncation error can be approximated as, $0.5(1-Cr)\Delta x\frac{\partial^2(Q^2/H)}{\partial x^2}$, where Cr is the local Courant number. By discretizing the truncation error terms and adding them to the upwind differencing it is possible to vastly improve the accuracy. This is important in this study which includes solitary wave propagation because it is the balance of the nonlinear amplitude dispersion terms with the frequency dispersion terms that maintains the permanent waveform.

3. RANS equation model

3.1. Governing equations

The Reynolds-averaged Navier–Stokes equations (RANS) can be written in Einstein's notation as:

$$\frac{\partial \gamma_i^a \overline{u}_i}{\partial x_i} = 0 \tag{4}$$

$$\frac{\partial \overline{u}_i}{\partial t} + \overline{u}_j \frac{\partial \overline{u}_i}{\partial x_j} = g_i - \frac{1}{\rho}\frac{\partial \overline{p}}{\partial x_i} + \frac{\partial}{\partial x_j}\left(\nu \frac{\partial \overline{u}_i}{\partial x_j} - \overline{u'_i u'_j}\right) \tag{5}$$

where $\overline{u}_i$ is the Reynolds-averaged flow velocity component in the i^{th} direction, g_i is the external force per unit volume, $\overline{p}$ is the Reynolds-averaged fluid pressure, ρ is the fluid density, ν is the kinematic viscosity, is the Reynolds averaging quantity, and $'$ is the fluctuation in the Reynolds average. γ^v is the void ratio of a computational cell, γ_i^a is the aperture ratio of a cell boundary in the i^{th} direction, and are used to enable the partial occupation of a computational cell with an object or bottom bathymetry which will be explained in §3.2. Finally, to close Eqs. (4) and (5), Boussinesq's assumption is made (Eq. (6)) and the standard eddy viscosity $k-\varepsilon$ model (Launder and Spalding, 1974) is used where the relevant equations are given as:

$$-\overline{u'_i u'_j} = \nu_t\left(\frac{\partial \overline{u}_i}{\partial x_j} + \frac{\partial \overline{u}_j}{\partial x_i}\right) - \frac{2}{3}k\delta_{ij} \tag{6}$$

$$\frac{\partial k}{\partial t} + \frac{\partial k\overline{u}_j}{\partial x_j} = \frac{\partial}{\partial x_j}\left[\left(\nu + \frac{\nu_t}{\sigma_k}\right)\frac{\partial k}{\partial x_j}\right] - \overline{u'_i u'_j}\frac{\partial \overline{u}_i}{\partial x_j} - \epsilon \tag{7}$$

$$\frac{\partial \epsilon}{\partial t} + \frac{\partial \epsilon\overline{u}_j}{\partial x_j} = \frac{\partial}{\partial x_j}\left[\left(\nu + \frac{\nu_t}{\sigma_\epsilon}\right)\frac{\partial \epsilon}{\partial x_j}\right] - C_{\epsilon 1}\frac{\epsilon}{k}\overline{u'_i u'_j}\frac{\partial \overline{u}_i}{\partial x_j} - C_{\epsilon 2}\frac{\epsilon^2}{k} \tag{8}$$

where, $\nu_t = C_\mu k^2/\epsilon$ is the turbulent viscosity, $k\left(\equiv \overline{u'_i u'_i}/2\right)$ is the turbulent kinetic energy, $\epsilon\left(\equiv \nu\overline{\frac{\partial u'_i}{\partial x_j}\frac{\partial u'_i}{\partial x_j}}\right)$ is the energy dissipation rate, and δ_{ij} is the Kronecker delta. The constants in Eqs. (6) - (8) correspond to those of the standard $k-\epsilon$ model: $\sigma_k = 1.0$, $\sigma_\epsilon = 1.3$, $C_\mu = 0.09$, $C_{\epsilon 1} = 1.45$, and $C_{\epsilon 2} = 1.92$ (Launder and Spalding, 1974). Moreover, in order to model the free surface the Volume of Fluid (VOF) method is employed that utilizes the following equation for the advection of fluid, in terms of the cell volume fraction, F:

$$\frac{\partial \gamma^v F}{\partial t} + \frac{\partial \gamma_i^a F\overline{u}_i}{\partial x_i} = 0 \tag{9}$$

3.2. Numerical scheme

The numerical scheme follows that of (Yoneyama et al., 2002). Eqs. (4)-(9) are discretized and solved on a staggered grid, yielding the first-order Euler, third-order upwind and second-order central difference discretizations for time, convection and all other terms respectively, with the stencil shown in Fig. 2 and difference formulas in Appendix B. The numerical procedure for pressure–velocity coupling is based on the Simplified Marker and Cell (SMAC) algorithm. Here, an initial velocity field, u^* is guessed using the previous values of $\overline{u}$, $\overline{p}$ and $\overline{u'_i u'_j}$ (or rather, a new value of ν_t after inserting Eq. (6) into (5) and rearranging) in Eq. (5). The resulting residual error, ε_D using the guessed velocity field in Eq. (4) is used to correct the pressure in the following Poisson pressure equation and obtain the updated solenoidal velocity field:

$$\overline{u}_i = u_i^* - \frac{1}{\rho}\frac{\partial \psi}{\partial x_i} \tag{10}$$

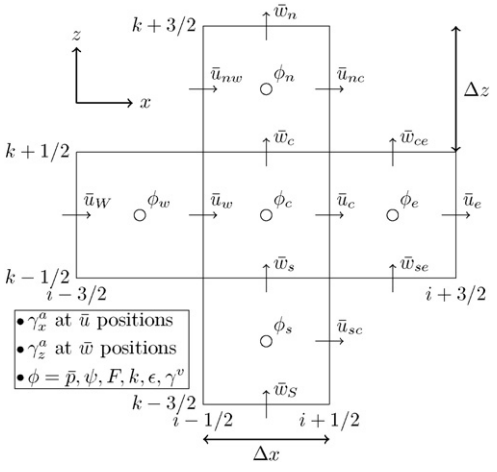

Fig. 2. Finite difference stencil in space for the RANS model scheme (Yoneyama et al., 2002).

$$\frac{\partial}{\partial x_i}\left(\frac{1}{\rho}\frac{\partial \psi}{\partial x_i}\right) = \frac{\partial u^*}{\partial x_i} = \epsilon_D \tag{11}$$

in which ψ is the potential function that is solved to give the required pressure correction. Eq. (11) is solved using a biconjugate gradient stabilized (BiCGSTAB) matrix solver. The solenoidal velocity field is used to solve the $k-\epsilon$ transport equations (Eqs. (6)-(8)) which will yield a new value of ν_t for use in the momentum equations.

Concerning the VOF procedure, Piecewise linear interface calculation (PLIC) (a variant on (Youngs, 1982)) is used to put Eq. (9) into practice using the updated solenoidal velocity field. This is achieved by first calculating the slope of the outward normal unit vector, $\vec{n} = -\nabla F/||\nabla F||$. The free parameter in the vector equation is solved by preserving F in the cell and used to find the vertices of the free surface within a computational cell. This information is used to transport the volume fraction more exactly than traditional VOF methods that only consider horizontal or vertical surfaces (simple line interface calculation). Furthermore, an improved Fraction of Volume Obstacle Representation (FAVOR) method is utilised, whereby the actual planar structure of an object or topographical surface is specified within a computational cell. This means that even in free surface cells that are partially occupied by an object (see Fig. 3) the correct slope and position of the free surface interacting with the object may be considered.

4. Two-way coupling method

The long wave (NSWE) model, and the RANS model presented in §2 and §3 respectively, are tightly two-way coupled to form the single 2CLOWNS model. The simulation proceeds by exchanging information at the interface region between the two constituent models. The method assumes that the inviscid irrotational long wave assumption is valid at the interface so that both models are calculating similar physics. The grid systems of each are overlapped by one cell width of the NSWE model (assumed equal to or of coarser resolution than the RANS model) as shown in Fig. 4.

4.1. RANS boundary condition

The boundary condition for the RANS domain most importantly requires knowledge of the vertical distribution of the horizontal velocity, $\overline{u}_{c,k}$, and the vertical velocity, $\overline{w}_{c,k}$ at the domain interface, where the k refers to a cell number in the vertical direction. This profile must be obtained from the volume fluxes, Q in the NSWE model. Furthermore, values of the fluid volume fraction, $F_{c,k}$ as well as the turbulent

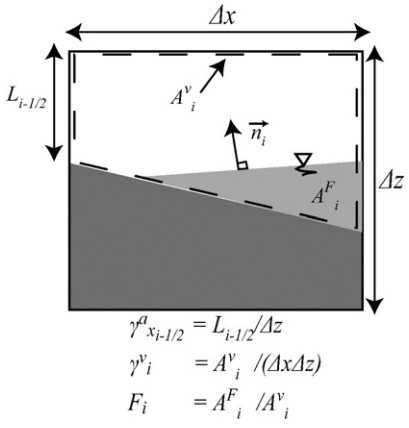

Fig. 3. Illustration of a computational cell that has a sloping free surface intersecting with the bottom topography; a possibility within the improved FAVOR method adopted in this study.

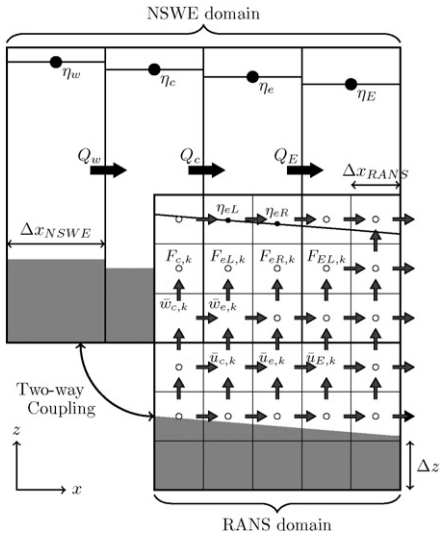

Fig. 4. Interface region between the NSWE and RANS model in 2CLOWNS with the necessary variables required for coupling.

quantities $k_{c,k}$ and $\varepsilon_{c,k}$ are also required. A description of these boundary conditions and how to obtain them is described in this section.

4.1.1. Horizontal velocity

The horizontal velocity defined on the interface between the NSWE and RANS model is a driving boundary condition to the RANS model since it is responsible for the correction of the pressure through continuity on the water column adjacent to the boundary. Thus, it is inserted as $\overline{u}^{n+1}_{c,k}$ and $\overline{u}^{*}_{c,k}$, i.e. it is the correct Solenoidal velocity after the time step *and* it is used as the "guessed" velocity in the Poisson Pressure equation (see Appendix B). The previous value, $\overline{u}^{n}_{c,k}$ may be used to evaluate the momentum equation as normal.

Referring to Fig. 4, Q_c, h_c are the flux and initial water depth on the boundary to the RANS model respectively, and η_c, η_e are the water levels in the cell centres adjacent to the boundary. The depth-averaged normal velocity, U_c can thus be found by:

$$U_c = \frac{Q_c}{(\eta_c + \eta_e)/2 + h_c} \tag{12}$$

The problem now becomes one of transforming U_c onto some vertical profile for $\overline{u}_{c,k}$ to use as a boundary condition for the RANS model. The simplest choice is the shallow water assumption that the horizontal velocities are uniform over the depth:

$$\overline{u}_{c,k} = U_c \tag{13}$$

In order for this assumption to be valid the flow in the RANS model should obey the true long wave assumptions so that the vertical profile of the horizontal velocities become close to uniform at the boundary. This may require the domain of the RANS model to be large enough so that reflections with rotations and non-hydrostatic effects inside the RANS domain do not return to the boundary which sometimes may be quite a restriction. One method to alleviate this strictness at the boundary is to introduce an arbitrary velocity distribution so that vortices rotating in the vertical plane may freely cross the boundary in the form:

$$\overline{u}_{c,k} = U_c + U'_{c,k} \tag{14}$$

where $U'_{c,k}$ is the fluctuation from the depth-averaged velocity as illustrated in Fig. 5.

Following (Fujima et al., 2002), a suitable boundary condition is obtained by setting the difference in U' across the boundary to zero (no

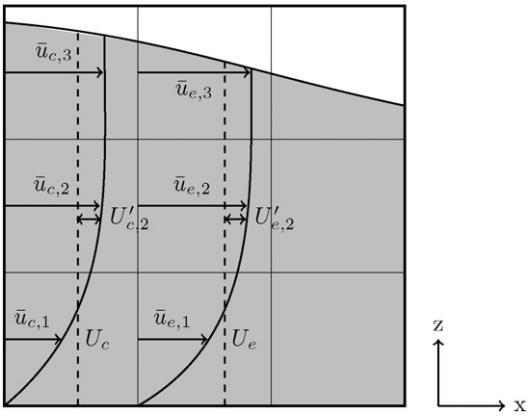

Fig. 5. Illustration of the arbitrary velocity profile based on no-gradient of the fluctuation, U' from the depth-averaged component, U.

gradient condition on U'). This means equating $U'_{c,k}$ to $U'_{e,k}$ in Fig. 4. Finally, the equation for $\bar{u}_{c,k}$ can be written as:

$$\bar{u}_{c,k} = U_c + \frac{\gamma^a_{xe,k}(F_{eL,k} + F_{eR,k})}{\gamma^a_{xc,k}(F_{c,k} + F_{eL,k})}(\bar{u}_{e,k} - U_e) \tag{15}$$

The ratio of the F volume fractions and aperture ratios, γ^a_x exists to ensure that the volume flux, Q_c is conserved.

4.1.2. Vertical velocity

The shallow water profile for the vertical velocity, $\bar{w}$, is found by integrating the continuity equation assuming a uniform horizontal velocity profile, and applying the kinematic boundary conditions at the sea bed and free surface. This results in a linear profile:

$$\bar{w}(z) = -\frac{\partial U}{\partial x}(z + h) \tag{16}$$

where z is the elevation from the initial undisturbed free surface. Note that even assuming a Boussinesq type profile of the horizontal velocities (quadratic) would result in a linear profile for the vertical velocities after ignoring terms of $O(\mu^4)$ (Sitanggang and Lynett, 2010). Eq. (16) implies that the vertical velocities depend on the gradient of the depth-averaged velocities which are found from the volume fluxes and the water depths. Referring to Fig. 4, a combination of U_w, U_c, and U_E must be considered in order to compute $\frac{\partial U_c}{\partial x_c}$. After evaluation of those depth-averaged velocities $\bar{w}_{c,k}$ can be determined by:

$$\bar{w}_{c,k} = -(z_k + h_c)\left[\frac{1}{(\Delta x_{NSWE})^2}(\Delta x_{RANS}U_c + (\Delta x_{NSWE} - \Delta x_{RANS})U_E/2 - (\Delta x_{NSWE} + \Delta x_{RANS})U_w/2)\right] \tag{17}$$

where z_k is the elevation from the initial free surface at the vertical cell integer k, and h_c is the initial water depth of the water column where $\bar{w}_{c,k}$ is defined (cell centre in terms of the horizontal plane). However, if an arbitrary profile of the horizontal velocities is specified (Eq. (15)) to account for the reflected waves with some rotation, the linear assumption of the vertical velocities could become a poor approximation to the RANS profile near the boundary. In this case, a no gradient boundary condition for $\bar{w}_{c,k}$ may be more appropriate:

$$\bar{w}_{c,k} = \bar{w}_{e,k} \tag{18}$$

4.1.3. Scalars

The free surface level is defined inside the boundary on cell C in terms of the cell volume fraction, $F_{c,k}$. This ensures that the correct volume flux is transported into the domain via the VOF method. $F_{c,k}$ is determined from the interpolation of η_c and η_e in the NSWE model:

$$F_{c,k} = \begin{cases} 0, & \text{if} z_k \geq \eta^*_c, \\ 1, & \text{if} z_{k+1} \leq \eta^*_c, \\ (\eta^*_c - z_k)/\Delta z, & \text{otherwise} \end{cases}$$
$$\eta^*_c = \left(\frac{\Delta x_{NSWE} + \Delta x_{RANS}}{2\Delta x_{NSWE}}\right)\eta_c + \left(\frac{\Delta x_{NSWE} - \Delta x_{RANS}}{2\Delta x_{NSWE}}\right)\eta_e \tag{19}$$

The remaining scalars that must be defined inside the boundary on cell C are the turbulent ones, k_c and ϵ_c. Since, the NSWE model is inviscid it provides no knowledge of these quantities and a no gradient boundary condition is applied:

$$k_{c,k} = k_{e,k} \quad \epsilon_{c,k} = \epsilon_{e,k} \tag{20}$$

As mentioned at the beginning of this section, it is assumed that the turbulence is negligible in the region where the models are coupled.

4.2. Long wave boundary condition

The boundary condition for the NSWE domain requires knowledge of the fluxes and free surface up to the edge of the finite difference stencil. That is, the necessary quantities to determine the flux, Q_c as indicated in Fig. 4. When calculating Q_c, the pressure gradient term requires η_e, and the dispersion correction procedure requires the dispersion potential function, ψ_e which itself requires both η_e and η_E and the value of Q_E from the predictor step (without dispersion) for computation. The predictor value of Q_E also only needs free surface information up to η_E in the pressure gradient terms so this marks the edge of our stencil. As the free surface level in the RANS domain is stored in the information of the surface cell, it only requires that the surface cell is found in the water column which is appropriately flagged for easy access. Further, averaging is required when resolution is different between model domains. For example, η_e in Fig. 4 can be found through:

$$\eta_e = \frac{\sum_{i=1}^{n}\eta_i}{n} \tag{21}$$

where n is the number of RANS cell centres that fall within the bounds of the cell e defined in the NSWE model and η_i is the free surface at the cell centre, i in the RANS model. This would simplify to $\eta_e = 0.5(\eta_{eL} + \eta_{eR})$ in Fig. 4. To calculate the nonlinear advection term, both the total water depths at the cell interface and the upwind fluxes are required. The water depths are easily obtained from the free surfaces and averaged using the method described in Appendix A. For the fluxes, in the case that $Q_c < 0$, Q_E is required in the upwind discretization of the advection terms and is calculated through the following operation:

$$Q_E = \Delta z \sum_{k=1}^{ke}\left(\gamma^a_{xe,k}u_{E,k}(F_{eR,k} + F_{EL,k})/2\right) \tag{22}$$

in which $k \in [1, ke]$ is the vertical cell integer and ke is the total number of vertical cells. Note that Eq. (22) does not depend on the ratio of Δx_{NSWE} and Δx_{RANS}, rather the average of F is just required across the cell boundary.

4.3. Calculation procedure

The procedure is best described by providing an example of stepping through one time step. Assume that all information is known at some time $t = t_n$ and the time step, Δt in both models is the same for

simplicity. Note the time staggering in the NSWE model of the free surface so they are defined at $t = t_{n+1/2}$ instead of $t = t_n$ for the fluxes:

1. Using $\eta^{n+1/2}$ and Q^n calculate the new fluxes, Q^{n+1} inside the NSWE domain through Eq. (2).
2. Pass the flux information, Q^{n+1} at the RANS boundary and convert to both a horizontal (Eqs. (13) or (14)) and vertical velocity distribution (Eqs. (17) or (18)). F^n in the ghost cells beside the boundary is found from η^n (found from linear interpolation of $\eta^{n-1/2}$ and $\eta^{n+1/2}$) in Eq. (19). A zero gradient boundary condition is applied to k and ϵ.
3. Using $\overline{u}^n, \overline{w}^n, p^n, \nu_t^n$ in the computational domain and $\overline{u}^{n+1}, \overline{u}^n, \overline{w}^n$ at the boundary, calculate u^*, w^* through Eq. (5).
4. Using u^*, w^* in the computational domain and $\overline{u}^{n+1}$ on the boundary, get $p^{n+1}, \overline{u}^{n+1}, \overline{w}^{n+1}$ through the Poisson pressure correction for a divergence free velocity field.
5. Get F^{n+1} through the advection of fluid Eq. (9). Update the new free surface level and normal vector using F^{n+1}.
6. Using k^n, ϵ^n, $\overline{u}^{n+1}$, $\overline{w}^{n+1}$ calculate k^{n+1}, ϵ^{n+1} explicitly in the $k-\epsilon$ transport Eqs. (6)-(8).
7. In the interface region, sum $\overline{u}^{n+1}$, F^{n+1} to get Q^{n+1} as described in Eq. (22). Find η^{n+1} through Eq. (21).
8. Using $\eta^{n+1/2}$ and Q^{n+1} in the long wave domain, calculate the new free surfaces, $\eta^{n+3/2}$ in the continuity Eq. (1). Repeat from step 1 for a new time step.

Note that, in this procedure at step 7 only η^{n+1} can be found in the RANS domain, whereas $\eta^{n+3/2}$ is actually required as calculated normally through continuity in step 8. This is corrected by adding a half time step of continuity to update η^{n+1} to $\eta^{n+3/2}$ explicitly in the interface region using the fluxes, Q^{n+1} passed from the RANS model. The correction was not found to have a large effect on the solution in general.

4.4. Consideration of different temporal resolution

Due to the often differing spatial resolution and disparate numerical schemes between the models, different temporal resolution between models may also be desired. Assuming that temporal resolution in the NSWE model is coarser than in the RANS model and of some integer multiple, this is easily achieved by looping over the the calculation of the RANS model $m = \Delta t_{NSWE}/\Delta t_{RANS}$ number of times per one time step of the long wave model. At the beginning of each loop of the RANS model, the depth-integrated flux from the NSWE model is linearly interpolated in time:

$$Q_c^{n+i/m} = \frac{m-i}{m} Q_c^n + \frac{i}{m} Q_c^{n+1} \tag{23}$$

where $i \in [1, m]$ is the loop number. $Q_c^{n+i/m}$ is the flux used to determine the velocity distribution for the boundary condition at the current time step in the RANS domain. After loop, $i = m$ of the RANS model, the free surface and flux information is exchanged back to the NSWE model for the next full time step. This exchange back to the NSWE model is not required when $i \neq m$.

5. Problem setup and model conditions

Shoaling of solitary waves on plane beaches has been extensively studied and is particularly useful for tsunami research and as a representation of short waves near breaking. Using 2CLOWNS, (Pringle and Yoneyama, 2014) showed a preliminary study for non-breaking solitary waves on a 1/20 slope. The model appeared to perform very well in terms of both the coupling and the prediction of free surface profiles, depth-averaged velocities and maximum runup for both the individual NSWE model and the coupled 2CLOWNS model simulating runup in the 2DV RANS domain. Furthermore, it was found that the results were not sensitive to the coupling position since the long wave assumptions are reasonable anywhere in the non-breaking tests. In this study breaking solitary waves are investigated to determine the limit of applicability and to examine if the coupled model can correctly reproduce breaking wave phenomena that is otherwise difficult or impossible for the NSWE model to reproduce.

5.1. Canonical problem definition and dimensionless variables

The canonical problem definition is sketched in Fig. 6. There exists a plane beach with slope s, where the origin of the x coordinate begins at the toe of the slope with x positive onshore of it. The offshore initial undisturbed water depth, h_0 is constant in the negative x direction of the toe of the slope. Thus, the initial undisturbed water depth, h is described by the following function:

$$\begin{cases} h = h_0 & \text{if } x \leq 0 \\ h = h_0(1 - xs) & \text{if } x > 0 \end{cases} \tag{24}$$

At some distance offshore of the slope, X_s at $t = 0$ there exists a permanent form solitary wave with offshore wave height, A_0. The free surface of the solitary wave is described by η, it is moving with wave speed, c and has horizontal and vertical orbital velocities, u and w respectively. Additionally, as the wave transforms over the slope the local wave height, A is constantly increasing until it breaks with a wave breaking height, A_b in an initial undisturbed water depth, h_b. It is customary to introduce dimensionless variables based on h_0 and g:

$$\begin{aligned} x' &= \frac{x}{h_0} \quad h' = \frac{h}{h_0} \quad A_0' = \frac{A_0}{h_0} \quad A' = \frac{A}{h_0} \quad \eta' = \frac{\eta}{h_0} \\ u' &= \frac{u}{\sqrt{g h_0}} \quad w' = \frac{w}{\sqrt{g h_0}} \quad t' = \frac{t}{\sqrt{h_0/g}} \end{aligned} \tag{25}$$

where $'$ indicates a dimensionless variable. The dimensionless variables will be used hereafter in the analysis. For consistency between numerical experiments we can define the distance X_s' to be equal to half a measure of the wavelength of a solitary wave which is arbitrarily defined here as containing 97.5% of the fluid volume according to Boussinesq's approximation (this is within 0.3% agreement to the length defined in (Synolakis, 1987)):

$$X_s' = \frac{2}{\sqrt{3A_0'}} \operatorname{arctanh}(0.975) \tag{26}$$

This ensures that waves go through the same distance before transformation up the slope. Additionally, in this study we wish to investigate a number of slopes and offshore wave heights in order to identify an applicable range of the 2CLOWNS model. A surf-similarity parameter is commonly used to collapse the beach slope and offshore wavelength (uniquely tied to a wave height for solitary waves) variables into one for analysis. In this study the slope parameter, S_0 introduced by (Grilli et al.,

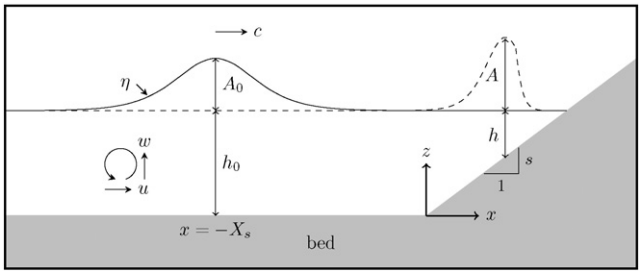

Fig. 6. Sketch of the canonical problem definition for solitary wave propagation, transformation and breaking on a plane beach.

1997) is adopted. It is defined as:

$$S_0 = \frac{s}{\mu_0} \tag{27}$$

where $\mu_0 (= h_0/L_0)$ is the inverse of the characteristic dimensionless length of the wave offshore for use in the slope parameter based on L_0:

$$L_0 = \frac{4h_0}{\sqrt{3A_0'}} \operatorname{arctanh}\left(\frac{\sqrt{3}}{3}\right) \tag{28}$$

which is equivalent to the length between the locations of maximum slope on the solitary wave. Thus, S_0 can be reduced to following expression for solitary waves:

$$S_0 = 1.521 \frac{s}{\sqrt{A_0'}} \tag{29}$$

5.2. Range of experimental conditions

Table 1 presents the matrix of dimensionless offshore wave heights, A'_0 and slopes with their corresponding value of S_0, and hence breaking type according to (Grilli et al., 1997). The waves are all plunging breakers which are the most interesting type to test complex breaking behaviour in the RANS model such as wave overturning, touchdown of the plunging jet, and splashup. The slopes from fairly steep to mild have been chosen because experimental and FNPF results are available for a comparison. For example, (Hsiao et al., 2008; Hwang et al., 2007) conducted experiments on the fairly mild 1/60 slope, (Grilli et al., 1994; Grilli et al., 1997) presents the most detailed data from the FNPF model on the intermediate 1/35 slope (since experiments were also conducted on this slope), and the (Synolakis, 1986) experiments were conducted on the fairly steep 1/20 slope. The mild 1/100 slope is also chosen because such slopes are common in tsunami cases.

5.3. Model conditions

In this study a total of four models are employed: the NSWE model, the RANS model, 2CLOWNS (combination of the previous two), and a FNBM (COULWAVE). Firstly, comparison of the individual constituent models of 2CLOWNS with each other is important to show where the strengths and weaknesses of each model lie. Secondly, their comparison with 2CLOWNS is important to see whether 2CLOWNS can do a good job of combining the best attributes of the NSWE model and the RANS model together. Thirdly, FNBMs have been shown to give good approximations of solitary wave shoaling in comparison with a FNPF model (Wei et al., 1995) and are very reliable for solitary wave propagation offshore. For shoaling before breaking starts to take place FNBM can be expected to give accurate solutions that may be taken to be the correct ones and plays the role of a "control model". Moreover, since the full RANS model takes a long time to compute, and is not so accurate for stable waveform propagation from far offshore, it is useful to compare the NSWE and 2CLOWNS solutions with the FNBM instead for parts of the analysis.

Grid sizes hereafter in the paper are equal to $\Delta x' = 0.05$ in NSWE and FNBM. The Courant number based on the wave speed is, $Cr = \sqrt{gh}\Delta t/\Delta x$ where $Cr \approx 0.20$ in FNBM and $Cr \approx 0.30$ in NSWE. In the RANS model they are, $1/80 \le \Delta x' \le 1/20$ and $\Delta z' = 1/80$. $\Delta x' = \Delta z'$ is set in the rapid shoaling region which was found to be important in order to get the required shoaling steepness here. The grid size is relatively unimportant offshore and in the gradual shoaling region. $Cr \approx 0.30$ based on the wave speed but during wave breaking, $Cr = u\Delta t/\Delta x$ based on the fluid velocity becomes dominant and is limited to $Cr = 0.1$ for stability. In the 2CLOWNS model the same grid size, $\Delta x' = 0.05$ is used in the NSWE domain while $\Delta x' = 1/80$ and $\Delta z' = 1/80$ is adopted in the RANS domain.

5.4. Permanent form solutions

The permanent form solitary wave numerical solution for each model is not known perfectly. Nevertheless, as an initial condition in the FNBM the weakly nonlinear dispersive solution of (Wei and Kirby, 1995) is used. For NSWE, a related solution in terms of depth-averaged velocities (Schember, 1982) is adopted. However, in both models there is a sudden initial decrease in the peak height before stabilization after a long enough simulation time due to the differences between the analytical and numerical solutions. Even after stabilization there may be further decrease due to numerical dissipation but this is found to be gradual and is within allowable errors. Notably, back substitution of the truncation terms in the upwind scheme of the NSWE model is required to mitigate dissipation errors. Moreover, a stable waveform could not be obtained in NSWE without this correction. Almost no recordable dissipation was recorded in FNBM after the stable waveform was obtained due to the high-order differencing.

Due to the initial decrease of wave profile in both models, the initial wave height on input to the model was tuned to give the desired permanent wave height. The resulting permanent waveforms of the FNBM and NSWE models for the range of A'_0 are plotted in Fig. 7 for comparison. Although little difference is noticeable for small values of A'_0, the wave profile is considerably narrower in the FNBM model as A'_0 increases. Since FNBM models have been shown to accurately reproduce waveforms (c.f (Wei and Kirby, 1995)) it must be concluded that the NSWE model loses accuracy in terms of reproducing the solitary waveform

Table 1
Matrix of slopes and offshore wave heights investigated in this study. The values in the cells indicate the value of S_0 and hence breaker types as written underneath.

Slope	Offshore wave height (A'_0)					
(s)	0.05	0.10	0.15	0.20	0.25	0.30
1/20	N/A	0.24	0.20	0.17	0.15	0.14
1/35	0.19	0.14	0.11	0.097	0.087	0.079
1/60	0.11	0.08	0.065	0.057	0.051	0.046
1/100	0.068	0.048	0.039	0.034	0.030	0.028

Note: $s = 1/20, A'_0 = 0.05$ case rejected.
Breakers types (Grilli et al., 1997):
$0.30 < S_0 < 0.37$: Surging breaker.
$0.025 < S_0 < 0.30$: Plunging breaker.
$S_0 < 0.025$: Spilling breaker.

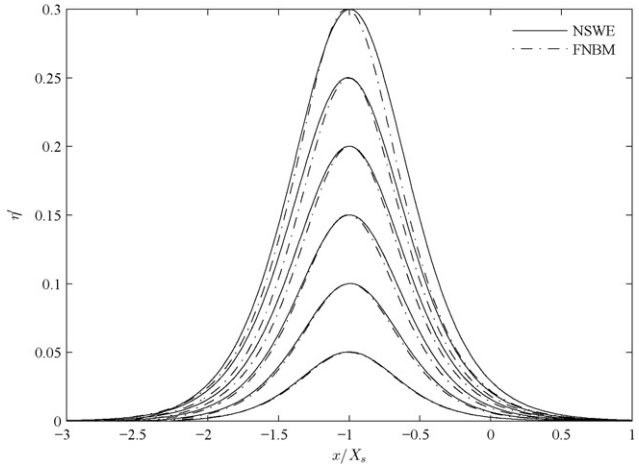

Fig. 7. Comparison of the offshore permanent waveform centred at $x = -X_s$ between the NSWE and FNBM models for the full range of offshore wave heights ($0.05 \le A'_0 \le 0.30$) investigated in this study.

for larger values of A_0'. The potential energy of the wave from the plots in Fig. 7 were calculated and it was found that the relative excessive error of potential energy in the NSWE model compared with FNBM is approximately 1.0% for $A_0' = 0.05$ but 10% for $A_0' = 0.30$. Hence it can be already recommended here that large values of A'_0 should be avoided when using the current 2CLOWNS model.

Concerning the RANS model, a permanent form solution is not pursued since it requires relatively large computational effort to simulate the wave offshore with sufficient resolution. In fact of course, this is one of the main drivers behind using the coupled 2CLOWNS model where it is computationally far more efficient and often more accurate to use the NSWE model offshore. Instead for purposes where a comparison is desired with the full RANS simulation, the wave is input at an offshore boundary suitably far from the toe of the slope (but close enough to reduce computational effort) using the (McCowan, 1891) higher order solutions detailed in (Munk, 1949).

5.5. Breaking mechanisms

Depth-integrated models require ad hoc methods to approximate the wave breaking processes. Two kinds of approaches are often employed. The first and perhaps more physical approach is to include some dissipative effect into the governing equations. FNBM adopts this approach and consists of an inbuilt eddy viscosity approximation (Kennedy et al., 2000) that is activated when the the gradient of the flux exceeds some threshold value. The second approach relies on the deactivation of dispersion terms when wave breaking is detected to prevent the anomaly of balancing amplitude dispersion with frequency dispersion in flux-dominated regions of flow (Roeber and Cheung, 2012). In this case, an empirical criterion to determine deactivation is required. For example, (Tonelli and Petti, 2009) suggests wave breaking can be detected when $A' > 0.80$. This is suitable for breaking waves on a flat bed or very mild slope although this can be far exceeded on steep slopes (Grilli et al., 1994). For this study a better approximation is used that incorporates the local surface gradient, s. (Camfield and Street, 1969) devised such an empirical formula for solitary waves on plane slopes: $A' > \max[0.75 + 25s - 112s^2 + 3780s^3, 0.8]$. However, it will be shown that the wave transformation in the zone of rapid shoaling is poorly approximated in the NSWE model. Hence it cannot accurately predict the wave breaking position despite being based on an empirical formula designed to approximate the situation at hand.

6. Intercomparisons of solitary wave shoaling on a Plane Beach

Comparisons between NSWE, full RANS, and FNBM (COULWAVE (Kim et al., 2009)) are investigated in this section to determine the applicable range of each model. The results of the comparison will be a guide to the limitations of each individual model and to determine the optimisation of coupling positions.

6.1. Individual model comparisons

This section compares solitary wave shoaling up to just beyond the point of decay (usually around the breaking point that can be defined as the point where the vertical tangent develops at the wave front) between the NSWE, FNBM and RANS models for five selected cases to show their individual strengths and weaknesses. The computation for the RANS model begins at the lateral boundary from $x' = -X_s'$ (see Fig. 6). In terms of computational time, for example on the fairly mild slope, $s = 1/60$ that should take quite long to compute in comparison to the steeper slopes, with $A_0' = 0.10$ the calculation took 423 min on an Intel Xeon 3.33GHz dual processor with six parallel threads (OpenMP) for 25 s simulation time. It should be kept in mind that the NSWE or even FNBM model can compute such calculations within a minute even from very far offshore (to allow for the permanent form solution to be obtained, c.f. §5.4). Additionally, significant numerical dissipation in the RANS model may occur just after the lateral boundary and when propagating from offshore for larger wave heights. These two points are the main disadvantages of the RANS model for wave applications that the 2CLOWNS model can ease. Moreover, such factors will of course be much greater in real tsunami applications which are calculated in 2DH/3D, and over much larger scales.

Fig. 8 plots the local wave height, A' versus the inverse of the dimensionless water depth, h_0/h for the five selected cases which are: (a) $A_0' = 0.05$ on $s = 1/100$ (b) $A_0' = 0.10$ on $s = 1/60$, (c) $A_0' = 0.15$ on $s = 1/35$, (d) $A_0' = 0.20$ on $s = 1/35$, and (e) $A_0' = 0.30$ on $s = 1/20$. For the mild slope cases shown in (a) and (b), all models demonstrate identical shoaling rates early on in the region known as the zone of gradual shoaling (Synolakis and Skjelbreia, 1993) that correspond well with Green's law ($\sim h^{-1/4}$). The FNBM and RANS model results start to diverge from those of the NSWE model where the deviation from Green's law is accentuated and the regime enters the zone of rapid shoaling (Synolakis and Skjelbreia, 1993), which is beyond $h_0/h \approx 3.5$ in (a) and $h_0/h \approx 2.3$ in (b). The behaviour of the NSWE model diverging as the regime in the FNBM model changes to rapid shoaling is noted for all the cases. It is clear that the RANS model accurately calculates this rapid shoaling rate as well which is in good agreement with the FNBM until these two models themselves diverge further along the slope. The divergence between the FNBM and RANS models are quite different depending on the slope. For the mild slopes $s = 1/100$ and $s = 1/60$, the RANS model will shoal far more rapidly in the final moments before breaking than the FNBM and break in similar water depths but with very different breaking wave heights. In contrast, as s is steepened, the FNBM model will start to shoal at similar rates on $s = 1/35$ and even more steeply on $s = 1/20$ just before breaking. In these cases, FNBM will predict breaking in much larger water depths than the RANS model in addition to smaller wave heights at breaking. Additionally, it is noted that as s is steepened, the rate of shoaling predicted by all three models is less steep than Green's law in the gradual shoaling region, which agrees well with the (Synolakis, 1986) experiments as can be seen on the steep slope (e), and as noted by (Grilli et al., 1994).

Overall, the initial shoaling characteristics of FNBM and the RANS model are shown to be comparable particularly in the regions leading up to the final transformation before wave breaking and decay of the waves deep inside the zone of rapid shoaling. Conversely, after the transition from the zone of gradual shoaling to the zone of rapid shoaling, the NSWE model cannot reproduce the required shoaling steepness that is shown by the FNBM and RANS models. It can be hypothesised that this is because of the low-order consideration of the nonlinear terms both analytically and numerically in the NSWE model. It would make physical sense that shoaling suddenly becomes rapid as nonlinear effects exceed some critical amount as the wave becomes gradually narrower. Beyond this critical location the nonlinear effects reinforce each other making the wave rapidly steeper and narrower until it destabilises and breaks.

6.2. Optimisation of the coupling position

This section investigates the shoaling disparities between the NSWE model and FNBM for the various wave heights and slopes to find a relationship between calculation conditions and an optimal coupling position. As demonstrated in §6.1, FNBM showed similar pre-breaking shoaling characteristics to the RANS model. In addition, (Wei et al., 1995) also presents excellent agreement of a fully nonlinear Boussinesq model with the FNPF model. Thus, FNBM is taken as a proxy for the correct pre-breaking shoaling characteristics to determine suitable coupling positions between the RANS and NSWE model since computations are much faster and generally more reliable in the FNBM model compared to the full RANS simulation. The idea is to identify the position on the slope where the solutions diverge indicating optimal positions for coupling in the 2CLOWNS model.

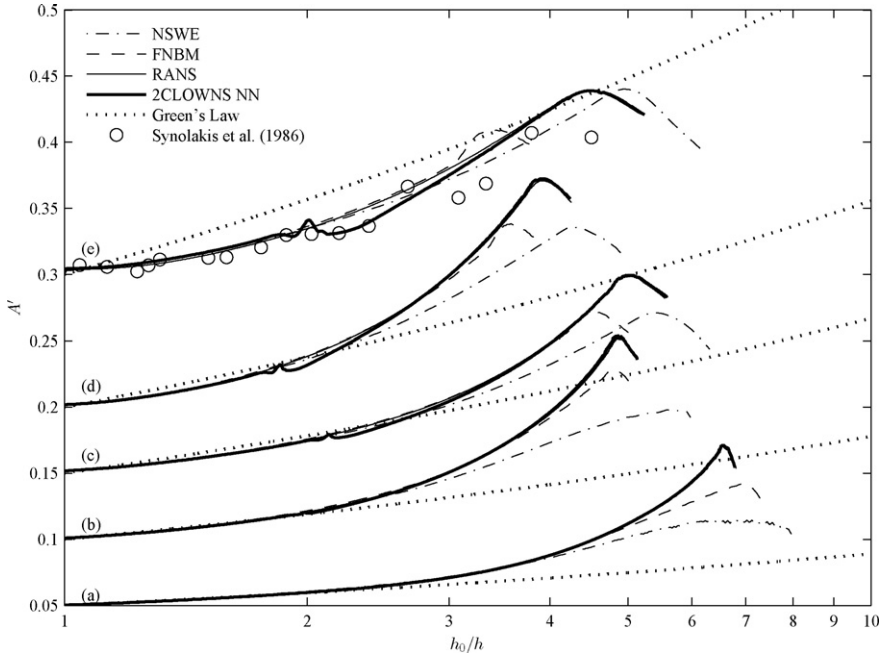

Fig. 8. Selected solitary wave transformation of the local wave height, A' versus h_0/h comparing: NSWE, FNBM, RANS and 2CLOWNS NN simulations, Green's law and (Synolakis, 1986) experiments in (e). (a) $A_0' = 0.05$, $s = 1/100$, (b) $A_0' = 0.10$, $s = 1/60$, (c) $A_0' = 0.15$, $s = 1/35$, (d) $A_0' = 0.20$, $s = 1/35$, (e), $A_0' = 0.30$, $s = 1/20$.

Plots of A' versus h_0/h are found in Fig. 9 for the entire range of variables shown in Table 1. In all cases it is observable that at some point along the slope the two numerical solutions diverge. This location is at larger values of h_0/h for lower values of A_0' and larger s. To obtain an empirical equation that describes the location where the two solutions diverge and hence a suitable coupling position, the absolute relative errors in A' between the two models were analysed versus h'. Since the solutions diverge in larger water depths for larger A_0' and milder slopes, the slope parameter, S_0 combining the two parameters is suitable that will convert the data into a function only of this variable. Through some combination of S_0 and A_0' ($S_0 A_0'^{-0.5}$), a logarithmic function was found to approximate the local water depth where the solutions diverge, h_c'. To get the exact equation an arbitrary cutoff of the relative error in local wave height between the models, $|A_{FNBM}' - A_{NSWE}'|/A_{FNBM}'$, was varied up to 7.5% to find best fits (least squares error). In general, the greater the cutoff of the error the better the fit which approached $R^2 = 0.995$. Cutoff errors smaller than 1% did not provide reliable equations. However, it is optimal to obtain an equation based on the position where the cutoff error approaches zero. To achieve this the coefficients in each reliable best fit equation ($R^2 > 0.98$) were extrapolated towards a cutoff error of zero. As a result the following equation was approximated:

$$h'_c = 0.16 - 0.25 \ln\left(S_0 A_0'^{-0.5}\right) \tag{30}$$

The resulting estimates of h'_c in Eq. (30) are included in Fig. 9 to indicate its effectiveness at estimating the divergence depth for each case. Taking the limits of h'_c to be 1 and 0, it is possible to determine lower and upper bounds of $S_0 A_0'^{-0.5}$ to be 0.035 and 1.9 respectively. For large incident wave heights and/or mild slopes with $S_0 A_0'^{-0.5} < 0.035$ coupling anywhere on the slope is unlikely to be accurate. While $S_0 A_0'^{-0.5} > 1.9$ means that coupling at any position on the slope is possible. In general, $S_0 A_0'^{-0.5} > 1.9$ corresponds to non-breaking or surging breakers so such a conclusion would appear valid. An additional note about Eq. (30) is that the deviation of the NSWE and FNBM models has been demonstrated to approximate the transition from the zone of gradual shoaling to the zone of the rapid shoaling (e.g. Fig. 8 (a), (b) deviation of FNBM from Green's law and NSWE both occur at similar locations). Thus, it may be possible to use Eq. (30) to estimate the location of the edge of the gradual shoaling zone as it transitions to the rapid shoaling region. However, further research into the validity of this claim is required.

7. Solitary wave shoaling and breaking on a Plane Beach using 2CLOWNS

§6.2 demonstrated that the NSWE model was reasonable up to a certain point along the slope before it diverged from the fully nonlinear Boussinesq model, FNBM. Eq. (30) was derived to give a suitable position for coupling to the RANS model based on a surf-similarity parameter so that shoaling errors are minimised while keeping the RANS domain as small as possible. In this section, initially the basic performance of the 2CLOWNS coupling for selected wave cases is shown in detail in §7.1. Verification of two-way coupling and the sensitivity to; the boundary condition for the RANS model, coupling position, and slope and offshore wave height on the performance of coupling is investigated. Following this 2CLOWNS was used to model all the solitary wave cases shown in Table 1 and the overall performance for pre-breaking shoaling is summarised.

One of the major advantages of using the RANS model contained within 2CLOWNS compared with a depth-integrated model is that it can simulate wave breaking without ad hoc dissipaters as well as the overturning wave shape. Moreover, it has advantages over FNFP flow models since it includes viscosity which may be significant for smaller scale waves, and it can model the post-breaking turbulent flow induced during the touchdown of the plunging jet, wave splash-up, bore propagation and resulting runup. With this in mind, this section demonstrates the ability of the 2CLOWNS model not only to reproduce rapid shoaling, but to also predict the wave breaking characteristics and the overturning wave shape. Comparisons are made against FNBM and FNFP flow models plus experimental observations where possible. In addition, vertical profiles of the velocities at selected locations are compared between NSWE and FNBM models to help explain the differences between the models. Analysis of the post-breaking turbulent flow and runup will be left to future studies.

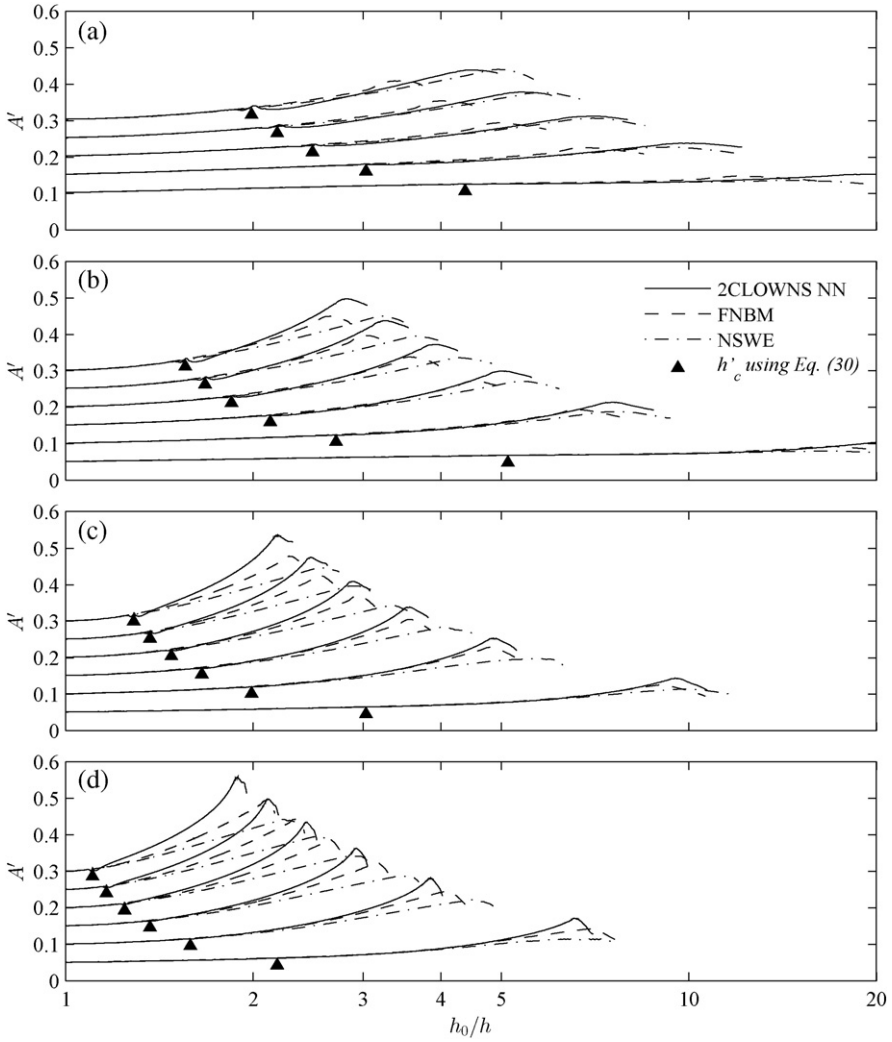

Fig. 9. Solitary wave transformation of the local wave height, A' versus h_0/h until breaking on various slopes for $A_0' = 0.05, 0.10, 0.15, 0.20, 0.25$ and 0.30 comparing 2CLOWNS NN, FNBM and NSWE simulations. (a) $s = 1/20$, (b) $s = 1/35$, (c) $s = 1/60$, (d) $s = 1/100$. Filled triangles indicate the water depth, h_c' where NSWE and FNBM are estimated to diverge - the depth where coupling in 2CLOWNS occurs - calculated using Eq. (30).

7.1. Basic evaluation of 2CLOWNS coupled model

This section summarises the basic performance of the coupling between the NSWE and RANS models. Three different aspects are investigated: a test of the two-way coupling and velocity boundary conditions, how the position (water depth) of coupling will affect the solution, and how the slope and offshore wave height can impact on the performance at the coupling interface.

Examples of the difference in calculation time between the singular RANS and 2CLOWNS simulations are summarised in Table. 2. The major contributor to the difference in the computational times is the reduction in the number of cells by coupling far up the slope reducing both horizontal and vertical cell numbers. Calculation times are shown for the time it takes for the wave to travel from $x' = -X_s'$ to far up the slope in small water depths ($h' = 0.10$). Hence this is a conservative comparison of the difference in calculation times expected during realistic scenarios when a wave may be propagated from far offshore. In such a case an even larger proportion of the calculation time will be reduced because during the initial propagation from offshore towards the slope only the NSWE model would be utilised until the wave reaches the RANS domain and the RANS model is switched on. For real tsunami simulations conducted in 2DH the potential for time reduction will be much greater given the size of the overall calculation domain beginning from possibly the tsunami source.

Table 2
Computational time taken for wave to travel from $x' = -X_s'$ to $h' = 0.10$ depending on RANS or 2CLOWNS simulations each conducted using six OpenMP threads.

Conditions		Simulation time (min)		Comparison (%)
s	A_0'	RANS	2CLOWNS	2CLOWNS/RANS
1/100	0.05	931	58	6.2
1/60	0.10	423	44	10
1/35	0.15	64	12	19
1/35	0.20	92	20	22
1/20	0.30	44	5	11

In addition, the ratio of spatial and temporal resolution between the NSWE and RANS models was, $\Delta x_{NSWE}'/\Delta x_{RANS}' = 4$ and $1 < \Delta t_{NSWE}/\Delta t_{RANS} < 21$ respectively for all simulations. $\Delta t_{NSWE}/\Delta t_{RANS}$ may be initially equal to 1 because of the smaller depth in the RANS domain compared with the NSWE one balancing the difference in cell resolution. However, $\Delta t_{NSWE}/\Delta t_{RANS}$, became as large as 21 during violent wave breaking. It did not appear that the difference in model resolutions, particularly the temporal ones, produced negative effects on the coupling performance.

Table 3
Test combinations used to investigate the sensitivity to the RANS velocity boundary condition in the two-way coupling algorithm.

Case Name	uniform $\overline{u}$	no gradient on U'	linear $\overline{w}$	no gradient on $\overline{w}$
2CLOWNS UL	✓		✓	
2CLOWNS UN	✓			✓
2CLOWNS NN		✓		✓

7.1.1. Two-way coupling and boundary condition test

A test of the two-way coupling algorithm and the sensitivity to the assumed velocity boundary condition to the RANS model is investigated in this section. The different combinations of the type of velocity profiles tested are defined in Table 3. Uniform u and no gradient on U' refer to Eqs. (13) and (14) respectively. Linear w and no gradient on w refer to Eqs. (16) and (18) respectively. Two test setups are adopted. One setup demonstrates pure reflection of solitary waves ($A_0' = 0.05$ and 0.15) against a vertical wall where coupling in 2CLOWNS takes place on a flat bed a distance $x' = 5$ from the wall. The second setup demonstrates coupling on the steepest slope investigated in this study ($s = 1/20$) at the coupling position determined from Eq. (30). $A_0' = 0.15$ is used as the incident wave height which gives the coupling depth to be $h_c' = 0.33$ ($h_0/h_c = 3.03$).

The results of the first setup for pure reflection against a vertical wall is summarised in Fig. 10. For both waves ($A_0' = 0.05$ and 0.15), snapshots of the reflected and incident waveforms with the wave peak centred on $x' = 0$, 5, 10 are shown to be in good agreement with each other for all simulations (RANS, 2CLOWNS NN and 2CLOWNS UL). The time series of η' at the same three locations also confirm the symmetry of the calculation. The larger wave height, $A_0' = 0.15$ shows greater disparities between the 2CLOWNS simulations and the full RANS one than for the $A_0' = 0.05$ case. However, the waveform for the incident wave centred on $x' = 0$ is already noticeably narrower in the RANS model than the waveform coming from the NSWE model. This fact has already been discussed in §5.4 comparing the NSWE and FNBM solutions, where it was found that the potential energy of the wave is greater in the NSWE model. Comparing the snapshots of the waveform at $x' = 0$ between the incident and reflected waves for $A_0' = 0.15$ shows that the wave height has slightly increased and the waveform has become slightly narrower after reflection in the 2CLOWNS simulations. This is consistent with the conservation of wave energy while the waveform has been slightly altered. In fact, the 2CLOWNS simulations have preserved the wave height marginally better than the full RANS simulation which suffers from greater numerical dissipation. From an overall perspective the disparities between the RANS and 2CLOWNS simulations do not appear to increase during the simulation confirming the robustness of the coupling algorithm. The other point to notice is that the results are not sensitive to the choice of velocity boundary condition (2CLOWNS UL or 2CLOWNS NN) in this test. This can be explained by the fact that coupling takes place on a flat bed with pure reflection of the wave so that the shallow water assumptions of the velocity profile should remain largely valid at the coupling interface even through the wave is reflected back from the RANS domain.

The results of the second setup on $s = 1/20$ is summarised in Fig. 11. Fig. 11(a) plots the evolution of A' across the coupling interface. Firstly, A' in the NSWE domain of the 2CLOWNS simulations is 0.002 larger than the full RANS simulation here because of the propensity for small dissipation in the RANS domain in comparison to depth-integrated wave models - it is worth mentioning that A' was identical between the models just offshore of the toe of the slope. During two-way coupling around the interface, a rise and drop of A' occurs before levelling off a short distance onshore. The 2CLOWNS UN and 2CLOWNS NN simulations give very similar results where a small hump in A' ($\approx$0.004 relative to the RANS result) occurs centred at the coupling interface before A' returns to a value similar to the full RANS simulation at $h_0/h \approx 3.2$. In contrast, the 2CLOWNS UL simulation gives a large drop in A' ($\approx$0.006) around the coupling interface followed by a rise in A' ($\approx$0.006) further onshore where it remains larger than the full RANS simulation. Furthermore, Fig. 11(b) and (c) plot the time series of η' and Q' respectively at the coupling interface. Q' in the 2CLOWNS UL simulations is $\approx$4% larger while η' is $\approx$3% smaller than the full RANS simulations as the wave peak passes through the coupling interface. In comparison Q' is $\approx$0.5% smaller and η' is $\approx$2.5% larger than the full RANS simulation for the 2CLOWNS UN and 2CLOWNS NN cases. These results indicate that the sensitivity to the boundary condition on $\overline{w}$ becomes significant when coupling on steep slopes. In this case a no gradient condition on $\overline{w}$ gives more robust results than the shallow water linear assumption of $\overline{w}$. This can be explained by the fact that as the

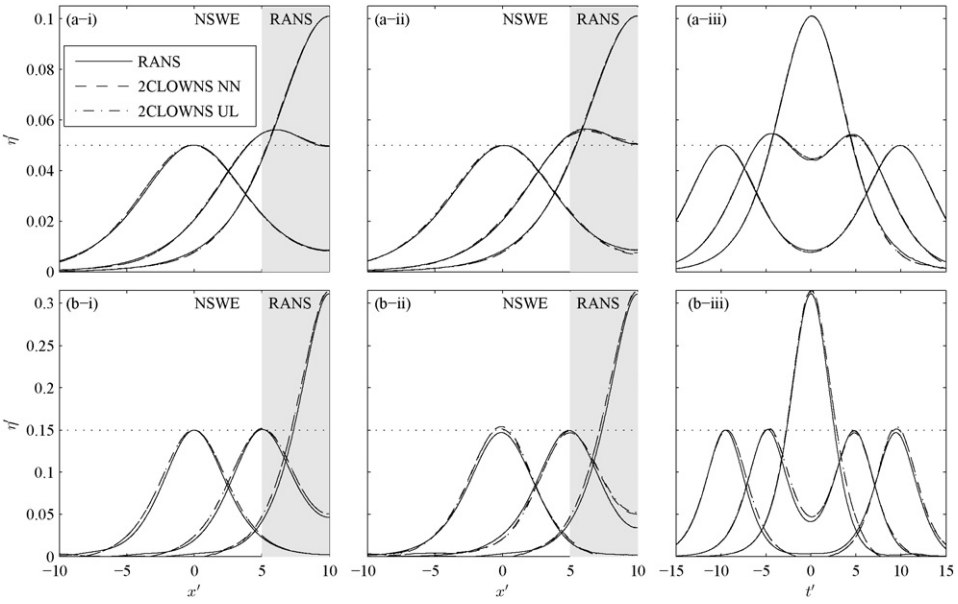

Fig. 10. Snapshots of the wave profile with wave peak centred on $x' = 0$, 5, 10, for (i) incident waves, and (ii) reflected waves; and (iii) time series of the free surface, η' at $x' = 0$, 5, 10 with $t' = 0$ corresponding to the time of maximum free surface at the vertical wall (located at $x' = 10$). Comparison is made between full RANS, 2CLOWNS NN and 2CLOWNS UL simulations where coupling takes place at $x' = 5$ in the 2CLOWNS simulations. (a) $A_0' = 0.05$, (b) $A_0' = 0.15$.

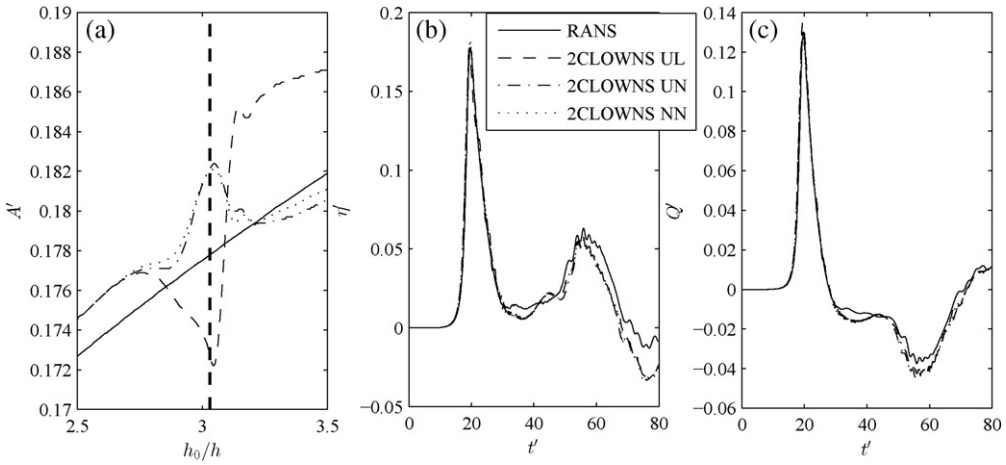

Fig. 11. Testing of 2CLOWNS two-way coupling (at $h_0/h_c = 3.03$) velocity boundary conditions (as summarised in Table 3) for $A'_0 = 0.15$ on $s = 1/20$ versus full RANS simulations; (a) evolution of the local wave height, A' around the coupling interface (indicated by vertical dashed line) for wave shoaling, (b) time series of η' at coupling interface, (c) time series of Q' at coupling interface. Time series includes the wave shoaling process for $t' < 40$ and the runup/rundown process for $t' > 40$.

wave enters the RANS domain the flow deviates slightly from the shallow water assumption where some of the wave is reflected back to the boundary from the slope. Particularly around the wave peak the errors associated with approximating the vertical velocity on the boundary can easily distort the wave. The no gradient condition on $\overline{w}$ is able to mitigate those distortions. In contrast, the distribution of $\overline{u}$ was not found to be important with regards to distortion of the wave and hence robustness of the two-way coupling. The no gradient condition on U' may still be useful however in the event that vertical vorticities cross the interface as demonstrated in (Fujima et al., 2002).

In Fig. 11(b) and (c), $t' > 40$ corresponds to the runup and rundown process. Overall the 2CLOWNS simulations show reasonable agreement with the full RANS simulations confirming that the two-way coupling algorithm is robust even for returning flow not related to pure wave reflection. The differences can be reasonably related to the increased energy of the incident wave in the NSWE model that results in greater magnitude of the return flow in 2CLOWNS (c.f Q' at $t' \approx 60$). For $t' > 40$ all three 2CLOWNS simulations demonstrate very similar behaviour with each other which could be explained by the fact that the incident wave energy that has entered the RANS domain is almost identical and because the return flow is not susceptible to distortion in comparison to the steep incident wave peak.

Given the results of the tests in this section the two-way coupling algorithm can be considered adequate to consider both incident and reflected waves. Furthermore, the 2CLOWNS NN boundary condition to the RANS model was found to give the most robust results hence this condition will be used for all subsequent simulations in this study.

7.1.2. Sensitivity to coupling position

In this section the effect of coupling at different positions or local water depths, h'_c is assessed. Two experimental combination are chosen: $A'_0 = 0.15$ on $s = 1/20$, and $A'_0 = 0.05$ on $s = 1/100$, to represent a fairly large wave on a steep slope and a small wave on a mild slope, respectively. Comparisons are made between coupling in 2CLOWNS NN at

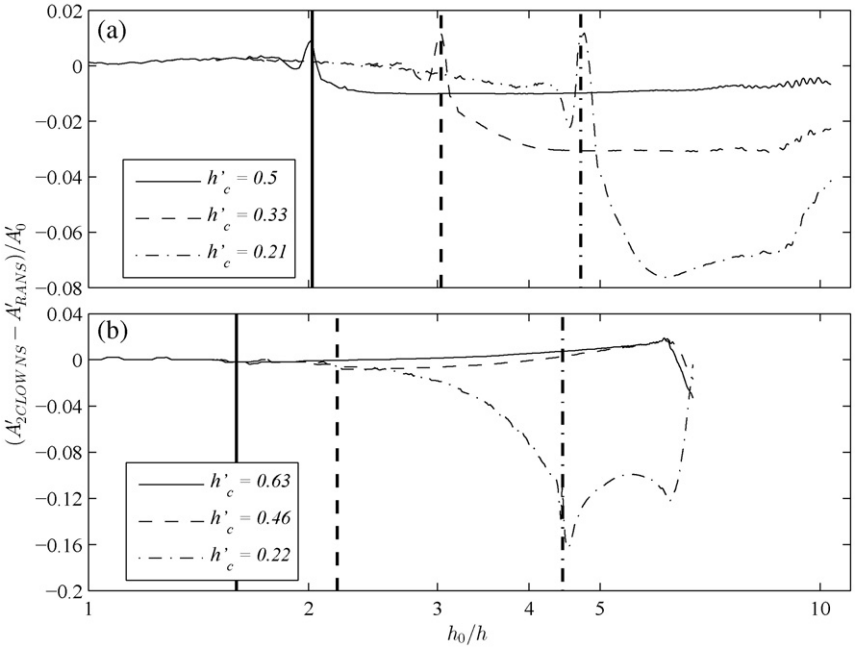

Fig. 12. Difference in the local wave height, A' normalised by A'_0 between 2CLOWNS NN and full RANS simulations until wave breaking. Coupling at three different depths for each slope (positions indicated by the vertical lines) are conducted where the middle depth is derived from Eq. (30) and the other two coupling depths are in between this location and; the toe of the slope and breaking point respectively. (a) $A'_0 = 0.15$ on $s = 1/20$, (b) $A'_0 = 0.05$ on $s = 1/100$.

three different values of h'_c. Eq. (30) is used to get the "optimal" h'_c for each slope. Two other test depths are used; 1) in between the toe of the slope and the optimal h'_c, and 2) in between the estimate of the breaking point and the optimal h'_c. Fig. 12 plots the difference in the local wave height normalised by A'_0 between the 2CLOWNS and singular RANS simulations during shoaling, i.e. $(A'_{2CLOWNS} - A'_{RANS})/A'_0$.

Fig. 12 shows that if coupling takes place in depths smaller than the optimal h'_c on each slope, initially the NSWE solution diverges far from the RANS one even before the coupling interface. At the coupling interface a hump-like increase and decrease in $A'_{2CLOWNS}$ occurs before extremely rapid shoaling takes place. The magnitude of the increase and decrease of $A'_{2CLOWNS}$ around the coupling location is larger for smaller coupling depths. When coupling in depths larger than the optimal, $A'_{2CLOWNS}$ tends to stay closer to the A'_{RANS} solution overall. In the case of $A'_0 = 0.15$ on $s = 1/20$, $A'_{2CLOWNS}$ near the breaking point is 1.6% closer to the A'_{RANS} solution where coupling takes place in large depths ($h'_c = 0.50$) rather than the optimal ($h'_c = 0.33$). On the other hand, for $A'_0 = 0.05$ on $s = 1/100$, $A'_{2CLOWNS}$ near the breaking point is essentially identical when coupling at either the optimal depth ($h'_c = 0.46$) or the larger depth ($h'_c = 0.63$). A small decrease in $A'_{2CLOWNS}$ (<1%) occurs when coupling at the optimal depth around the coupling interface but this is not evident when coupling at the larger depth. This is offset by a significantly faster computational time and the ability to estimate breaking at the same location in the end. For tsunami-like problems with mild slopes and small wave heights coupling at the depths predicted by Eq. (30) appears reasonable but when coupling on steeper slopes a case can be made that coupling in greater depths is preferred.

7.1.3. Sensitivity to slope and offshore wave height

To get a brief idea of the performance of 2CLOWNS with different slopes and offshore wave weights, snapshots of the waveform where the peak is centred on the coupling position are shown in Fig. 13 comparing NSWE, RANS and 2CLOWNS simulations. Fig. 13 (a) plots $A'_0 = 0.05$ on $s = 1/60$, and the waveform conforms excellently to both the NSWE and RANS model profiles indicating that the coupled model is particularly adept for small wave heights and slopes. Note that this case is in general a good representation of typical tsunami situations in the field (small nonlinearity and a mild slope). Fig. 13 (b) and (c) plots snapshots of the wave peak for the two other examples; $A'_0 = 0.15$ on $s = 1/35$, $A'_0 = 0.30$ on $s = 1/20$. As previously shown the NSWE waveform is wider than the RANS one as A'_0 increases. It is noticeable how the 2CLOWNS waveform tends to the NSWE one whose input data has of course been used to generate the solitary wave in the RANS domain. However, the 2CLOWNS waveform does deviate slightly from the NSWE profile particularly inside the RANS domain.

All the experimental cases were simulated using 2CLOWNS NN. The results of wave transformation until breaking is plotted in Fig. 9. In all cases there is a small hump in $A'_{2CLOWNS}$ at the coupling interface which is mostly noticeable for steeper slopes and larger A'_0. To better quantify this effect when adopting the optimised coupling location (Eq. (30)) for different slopes and offshore wave heights, the relative error of the local wave height in 2CLOWNS NN simulations against FNBM ones in the vicinity of the coupling interface, i.e. $(A'_{2CLOWNS} - A'_{FNBM})/A'_{FNBM}$, was calculated for all experimental combinations. The maximum value of $(A'_{2CLOWNS} - A'_{FNBM})/A'_{FNBM}$ around the interface, denoted A_{RE}, was calculated and the following empirical equation ($R^2 = 0.994$) was derived based on some combination of S_0 and s ($S_0 s^{-1.095}$):

$$A_{RE} = 0.132 \exp(-0.410 S_0 s^{-1.095}) \tag{31}$$

The negative exponential function of the parameter $S_0 s^{-1.095}$ in Eq. (31) implies that errors at the coupling interface increase with both s and A'_0. The effect of A'_0 on A_{RE} is significantly stronger than the effect of the slope ($A_{RE} \sim A'^{0.5}_0, s^{-0.095}$). It is probable that the dependency of Eq. (31) on s could in fact be removed by improving Eq. (30) to take into account the increased difficulty of coupling in the shallower depths that Eq. (30) prescribes on steeper slopes. Thus, the major errors associated with coupling are mostly due to the difference in the permanent waveforms between the governing equations. If high-order models such as the FNBM one is used instead of the NSWE model to couple with the RANS model (c.f. (Sitanggang and Lynett, 2010)) the coupling will most likely improve. However, it is stressed that for large values of $S_0 s^{-1.095}$ the use of the NSWE model is highly recommended given its efficiency in computation over wide areas and simplicity in grid nesting. This condition is also likely to be satisfied in most cases of tsunami and other long wave problems. For example, the minimum value of $A_{RE} = 0.0018$ occurs at the maximum value of $S_0 s^{-1.095} = 10.5$ ($A'_0 = 0.05$ and $s = 1/100$). Setting an arbitrary allowable limit on A_{RE} to 1% for

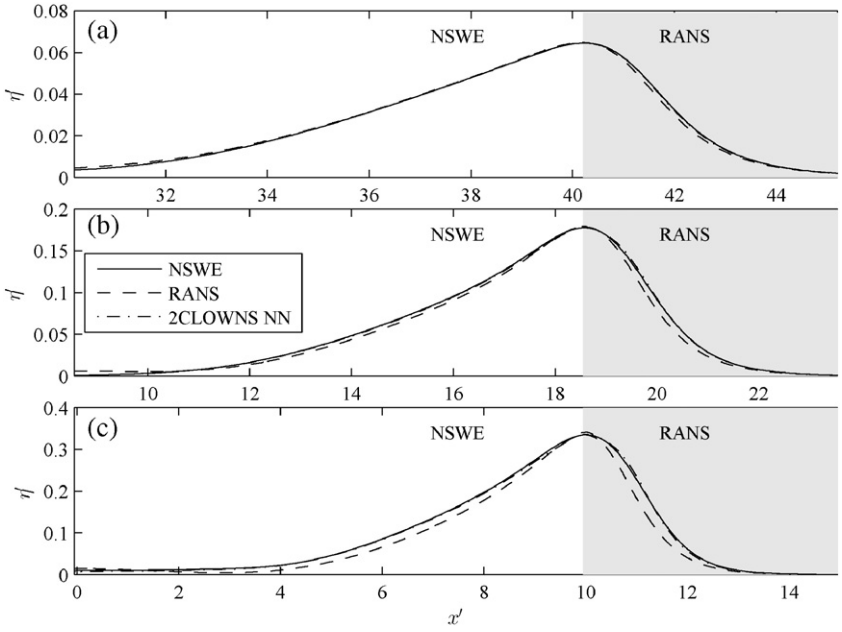

Fig. 13. Snapshot of the peak of selected solitary waves centred on the 2CLOWNS coupling position. NSWE, RANS and 2CLOWNS with shaded area indicating RANS domain in 2CLOWNS simulation. (a) $A'_0 = 0.05$, $s = 1/60$, (b) $A'_0 = 0.15$, $s = 1/35$, (c) $A'_0 = 0.30$, $s = 1/20$.

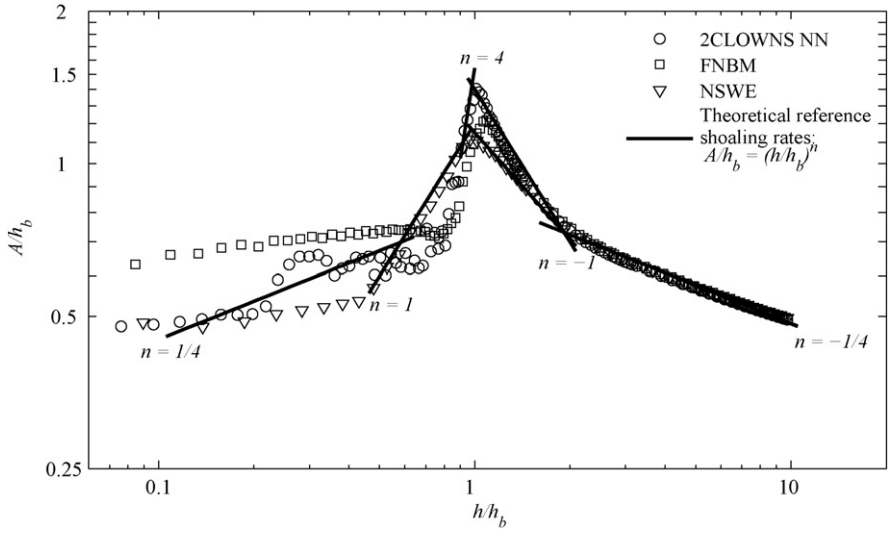

Fig. 14. Evolution of the local wave height of a solitary wave ($A'_0 = 0.05$) on a 1/60 slope comparing 2CLOWNS NN, FNBM, NSWE models with theoretical reference shoaling rates (Synolakis and Skjelbreia, 1993) included.

example would require $S_0 s^{-1.095} > 6.3$. This limits the offshore wave height to, $A'_0 \leq 0.103$ on the steepest slope ($s = 1/20$) and to, $A'_0 \leq 0.140$ on the mildest slope ($s = 1/100$) investigated in this study.

7.2. Pre-breaking shoaling performance

In this section the accuracy of the wave transformation prior to breaking is discussed. As an initial example the entire shoaling transformation plus post-breaking decay (covered in §7.4) of the 2CLOWNS NN simulation compared with the NSWE and FNBM models for the case with $A'_0 = 0.05$ and $s = 1/60$ is plotted in Fig. 14. The axes have been nondimensionlised by the water depth at breaking, h_b recorded in the 2CLOWNS model and a discussion of its estimation will take place in §7.3. Normalisation with h_b is to allow for easy comparison with the plot presented in (Hsiao et al., 2008) for $A'_0 \approx 0.05$ on the same slope. Expected shoaling rates from (Synolakis and Skjelbreia, 1993) are also plotted for reference (note that these are *not* best fit lines). In the zone of gradual shoaling the 2CLOWNS model utilises the efficient NSWE model and no major differences between any of the models is evident. Thereafter, in the transition region coupling takes place ($h'_c = 0.33 \rightarrow h/h_b = 3.22$) and the zone of rapid shoaling is modelled through the RANS calculation. The shoaling rate described by 2CLOWNS NN in this zone is shown to follow approximately that of FNBM both agreeing with Boussinesq's theoretical shoaling law ($\sim h^{-1.0}$). Agreement between the models continues up until $h/h_b \approx 1.1$ where wave breaking occurs in the FNBM prematurely in comparison to the 2CLOWNS NN simulation. The rate of rapid shoaling in the NSWE model is smaller than Boussinesq's law ($\sim h^{-0.7}$ instead).

Fig. 9 plots the transformation of A' for all the experimental conditions. It is demonstrated how the shoaling rate in 2CLOWNS NN generally increases against the FNBM result as the slope becomes milder and also as A'_0 increases. In particular, as s is steepened a larger dip in A' occurs that does not easily recover versus FNBM in comparison to the behaviour on mild slopes. This may simply be because of inherent disparities in shoaling rates between the RANS and FNBM models themselves rather than a coupling issue as Eq. (31), a function only weakly dependent on s, suggests. To demonstrate the effect of the two-way coupling process on the shoaling rate rather than the effect of the difference simply between the RANS and FNBM models, Fig. 8 plots a comparison of the wave transformation for 2CLOWNS NN in comparison with single model NSWE, FNBM, and RANS simulations. Particularly in plots (c) - (e) a dip in $A'_{2CLOWNS}$ around the coupling interface is noticeable. Despite this the solution is able to recover and excellent agreement between the singular RANS and 2CLOWNS NN simulations is shown close to the breaking point in all cases implying that the effect of coupling on the final solution (at breaking/post breaking which in this study only the RANS/2CLOWNS NN model can rigorously simulate) is minimal. Hence it is conjectured that most of the differences shown between FNBM and 2CLOWNS in Fig. 9 is simply due to actual differences between the RANS and FNBM models rather than the coupling process. Of course the 2CLOWNS solution does diverge from the correct one around the coupling interface to various degrees which itself may be undesirable. However, given sufficient room to recover, the final solution is considerably accurate.

7.3. Wave breaking characteristics

Prediction of the wave breaking characteristics is important to show the improved performance of the 2CLOWNS NN model over long wave models including higher-order ones such as FNBM. The breaking point is usually defined as the location where the wave front has a vertical tangent (Grilli et al., 1997). This can be accurately determined in the 2CLOWNS (RANS) model since the free surface normal in each computational grid is explicitly determined. Wave breaking is said to have occurred in the 2CLOWNS simulations once the horizontal component of the free surface normal vector in any cell around the wave face is larger than 0.999. The resulting values of the water depth at breaking, h'_b and the wave height at breaking, A'_b is then determined from the free surface profile at that exact snapshot in time.

Firstly, the example shown in Fig. 14 for $A'_0 = 0.05$ and $s = 1/60$ is analysed in detail. The value of h'_b in the 2CLOWNS NN simulation was found to be equal to $h'_b = 0.103$. To make a comparison the empirical formula for plunging breakers presented in (Grilli et al., 1997) based on their FNFP flow simulations is introduced:

$$h'_b = \frac{0.149}{(S_0/A'_0)^{0.523}}, S_0 < 0.3 \tag{32}$$

Eq. (32) gives $h'_b = 0.097$ for $A'_0 = 0.05$ and $s = 1/60$. The experiments of (Hsiao et al., 2008) on $s = 1/60$ were also found to be within good agreement to this equation particularly for $S_0/A'_0 > 2$ which is the case here (Eq. (32) slightly underestimates h'_b otherwise). 2CLOWNS gives a prediction of h'_b in this example to within 6.2% of Eq. (32). In comparison h'_b in FNBM can be estimated as $h'_b = 0.111$ based on the location of the maximum value of A' which is an overestimation of approximately 14%.

The other wave breaking characteristic of concern is the wave breaking index, A_b/h_b. In the 2CLOWNS NN simulation for $A'_0 = 0.05$ and $s = 1/60$ the local wave height at breaking is, $A'_b = 0.141$ (in comparison $A'_b = 0.126$ in FNBM). This is equivalent to a breaking index of $A_b/h_b = 1.37$. Again for a comparison, the (Grilli et al., 1997) empirical formula for the breaking index is as follows:

$$\frac{A_b}{h_b} = 0.841 \exp(6.421 S_0) \tag{33}$$

Eq. (33) gives $A_b/h_b = 1.74$ for $A'_0 = 0.05$ and $s = 1/60$. However, (Hsiao et al., 2008) note that for $S_0 > 0.10$ Eq. (33) may tend to overestimate A_b/h_b, and they found little deviation from $A_b/h_b = 1.1$ in all of their experimental cases. This is because h'_b is very small here and a slight variation will affect the A_b/h_b ratio significantly. Taking into account both Eq. (33) and the experimental results of (Hsiao et al., 2008) the "middle ground" estimation of $A_b/h_b = 1.37$ can be considered a reasonable result.

Based on all the experimental cases simulated by the 2CLOWNS model in this study, empirical equations are derived for the prediction of h'_b ($R^2 = 0.944$) and A_b/h_b ($R^2 = 0.964$) in a similar form to Eqs. (32) and (33):

$$h'_b = \frac{0.138}{\left(S_0/A'_0\right)^{0.664}}, S_0/A'_0 < 4 \tag{34}$$

$$\frac{A_b}{h_b} = 0.872 \exp(5.258 S_0), S_0 < 0.25 \tag{35}$$

where the upper limits of the data included in derivation of Eqs. (34) and (35) are shown. The data points are plotted in Fig. 15 along with the best fit (least-squares) curves corresponding to Eqs. (34) and (35). The curves corresponding to Eqs. (32) and (33) found in (Grilli et al., 1997) are also drawn for comparison.

Concerning the calculation of h'_b in Fig. 15(a), Eq. (34) is shown to match Eq. (32) fairly well overall particularly for $S_0/A'_0 < 1$. It is worth mentioning that Eq. (32) from (Grilli et al., 1997) was derived with only one data point for $S_0/A'_0 > 1$. In this study six cases of $S_0/A'_0 > 1$ is included which mostly likely accounts for the differences between Eqs. (34) and (32) in this region. It is noted that the values for larger $S_0/A'_0 > 1$ are more scattered than those in the $S_0/A'_0 < 1$ bracket as indicated by the 95% prediction interval. In fact the (Grilli et al., 1997) Eq. (32) lies well within the prediction interval thus it is difficult to make definitive conclusions on the superior accuracy of either Eq. (32) or Eq. (34) but in general fair agreement between the two equations are found.

The breaking index A_b/h_b is plotted in Fig. 15(b). Eq. (35) derived in this study is in good agreement with Eq. (33) from (Grilli et al., 1997) for small values of $S_0 < 0.1$. For $S_0 > 0.1$, A_b/h_b in this study is somewhat smaller than that described by Eq. (33). In fact, Eq. (33) lies outside the 95% prediction interval for $S_0 > 0.15$, thus it is unlikely to accurately describe the results in this study for large values of S_0. This may be because $S_0 > 0.3$ in (Grilli et al., 1997) corresponds to surging breakers which could have affected the slope of Eq. (33) over the interval $0.10 < S_0 < 0.25$ for plunging breakers where comparatively little data was available. In contrast all the wave types were plunging breakers in this study. As mentioned earlier, (Hsiao et al., 2008) indeed noted that Eq. (33) had a tendency to overestimate values of S_0 within this range.

7.4. Post-breaking behaviour and wave shape

As described in (Synolakis and Skjelbreia, 1993), after wave breaking the local wave height undergoes transformation according to a zone of rapid decay on the order of $\sim h^4$, followed by a zone of gradual decay $\sim h$. (Hsiao et al., 2008) also postulated that on their mild slope, $s = 1/60$ a fifth region corresponding to bore front propagation exists, where decay follows $\sim h^{1/4}$. Fig. 14 for $A'_0 = 0.05$ and $s = 1/60$ plots the 2CLOWNS NN data alongside expected shoaling rates. The rate of rapid decay is demonstrably in close agreement to the theoretical $\sim h^4$ rate. The rate of gradual decay appears slightly steeper than theoretically suggested but the data is quite scattered due to the overturning wave shape. The final bore front propagation region on average appears to follow the rate ($\sim h^{1/4}$) suggested by (Hsiao et al., 2008).

To give the readers an idea of the performance of the RANS model in terms of its ability to model the overturning wave shape, touchdown of the plunging jet and wave splashup, Fig. 16 shows snapshots of the breaking wave with $A'_0 = 0.20$ on $s = 1/35$. This case was chosen

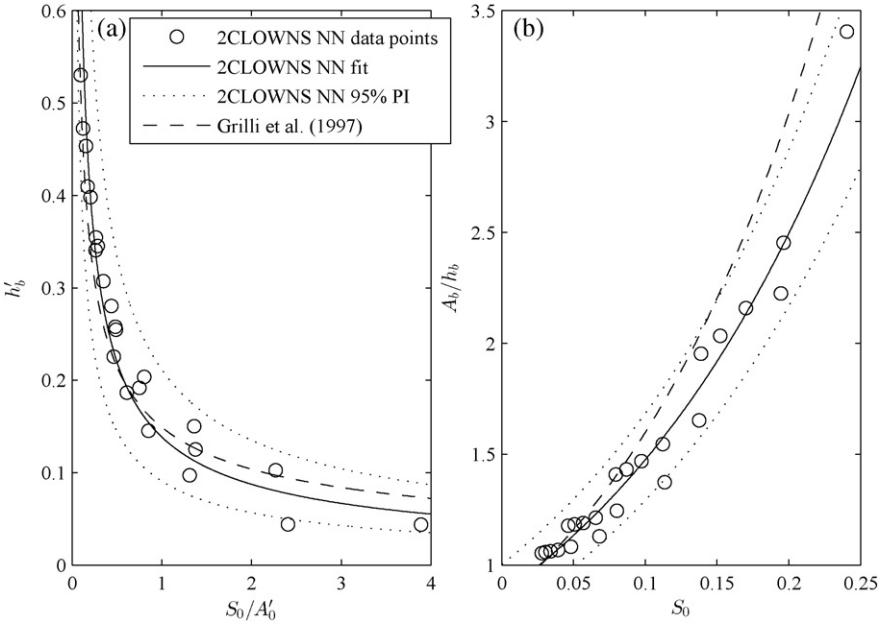

Fig. 15. Breaking criteria calculated in 2CLOWNS NN for all wave cases in this study with best fit curves and 95% prediction intervals (PI) compared to best fit curves calculated in (Grilli et al., 1997): (a) water depth at breaking, h'_b versus S_0/A'_0 with Eq. (34) - this study and Eq. (32) - (Grilli et al., 1997); (b) wave breaking index, A_b/h_b versus S_0 with Eq. (35) - this study and Eq. (33) - (Grilli et al., 1997).

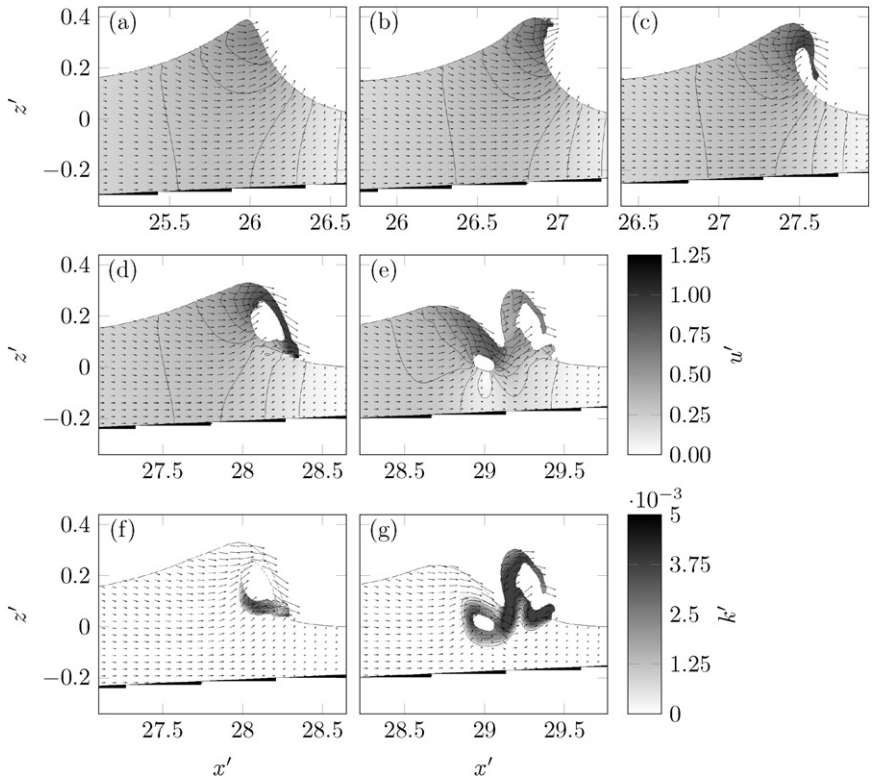

Fig. 16. Breaking wave shape and kinematic quantities (velocity magnitude, u' and turbulent kinetic energy, k') in the RANS domain of the 2CLOWNS model for $A'_0 = 0.20$ on $s = 1/35$: (a) prior to breaking (u'), (b) at the onset of wave breaking (u'), (c) formation of the plunging jet (u'), (d) touchdown of the plunging jet (u'), (e) wave splashup (u'), (f) touchdown of the plunging jet (k'), (g) wave splashup (k').

because illustrations are also found in (Grilli et al., 1997) for the exact same case that readers may refer to. Fig. 16 (a) - (e) plots snapshots of the wave shape at five different stages in the breaking phase along with velocity vectors and greyscale intensities of the normalised velocity magnitude, u'.

%For the online version only:

Also, a full animation of the wave transformation and breaking process in the RANS domain showing a colormap of u' is available in Video 1.

%end of online version.

The five different stages in order are; (a) wave shape prior to breaking, (b) at the onset of breaking, (c) the formation of the plunging jet, (d) touchdown of the plunging jet and, (e) wave splashup. Fig. 16 demonstrates that the RANS model in 2CLOWNS has the ability to at least qualitatively model the full process of wave breaking. The accuracy of the jet profile is strongly linked to the cell resolution and it is very difficult for the VOF model to get a beautifully smooth jet profile similar to those generated by the FNPF model as shown in (Grilli et al., 1997) without resorting to very fine grid sizes. Nevertheless, the RANS model appears to give a fair representation of the jet shape and it has the distinct advantage of modelling the touchdown of the plunging jet and wave splashup as shown in Fig. 16 (d), (e).

The normalised turbulent kinetic energy, k' is also shown for the same snapshots in Fig. 16 (f), (g)

%For the online version only:

- plus the wave transformation and breaking process in the RANS domain showing a colormap of k' is available in Video 2 -

%end of online version

demonstrating the onset of the turbulent flow that a FNPF model and in general depth-integrated models cannot simulate. The wave splashup in Fig. 16 (e), (g) is shown to contain three distinct regions of air (although the air flow itself is not computed) and counter-rotating vortices as illustrated through sketches and high quality photographs in (Li and Raichlen, 2003). Hence the model is shown to possess qualitative predictive ability to describe the full wave breaking process. Full quantitative analysis of the breaking process plus that of bore front propagation and wave runup will be undertaken in future studies.

7.5. Velocity profiles

In order to provide some explanation for the high performance of 2CLOWNS in comparison to NSWE and FNBM, velocity profiles for both u' and w' are plotted at four separate locations for $A'_0 = 0.05$ on $s = 1/60$, in Fig. 17. The locations correspond to the four zones of shoaling and decay introduced in (Synolakis and Skjelbreia, 1993). The vertical velocity profiles for u and w in NSWE are found from the following equations based on the weakly nonlinear Boussinesq assumption using the depth-averaged velocity:

$$u(z) = U + \left(\frac{1}{6}h^2 - 0.5(z+h)^2\right)\frac{\partial^2 U}{\partial x^2} \tag{36}$$

$$w(z) = -\frac{\partial U}{\partial x}(z+h) \tag{37}$$

Velocity profiles for FNBM are found from the equations based on a fully nonlinear Boussinesq assumption using the velocity at an arbitrary depth, z_α (Sitanggang and Lynett, 2010):

$$u(z) = u_\alpha + \frac{1}{2}\left(z_\alpha^2 - z^2\right)\frac{\partial^2 u_\alpha}{\partial x^2} + (z_\alpha - z)\frac{\partial^2 (h u_\alpha)}{\partial x^2} \tag{38}$$

$$w(z) = -\frac{\partial u_\alpha}{\partial x}z - \frac{\partial (h u_\alpha)}{\partial x} \tag{39}$$

The 2CLOWNS velocity profiles are taken directly from the RANS model.

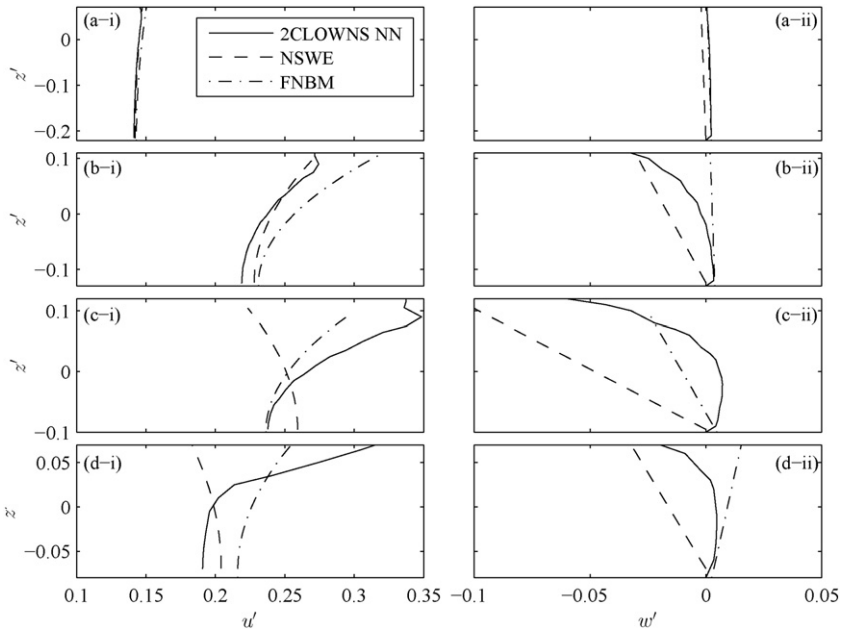

Fig. 17. Velocity profiles ((i) u' on left, (ii) w' on right) under the wave crest of a solitary wave ($A'_0 = 0.05$) on a 1/60 slope at four separate locations comparing 2CLOWNS NN, NSWE, and FNBM simulations; (a) $h/h_b = 2.1$, (b) $h/h_b = 1.2$, (c) $h/h_b = 0.93$, (d) $h/h_b = 0.68$.

First, at $h/h_b = 2.2$, Fig. 17 (a) confirms that all three models have good agreement for both u' and w' even at the edge of the zone of gradual shoaling where $h/h_b = 2.2 \rightarrow h' = 0.22$ is located. The magnitude of w' is small and the profile of u' has small curvature where u' at the free surface is only slightly larger than at the bed. It is these reasons that help explain why the NSWE model is just as accurate at predicting shoaling as the FNBM and RANS model in this zone, since the assumptions of the NSWE model are still valid.

However, in the zone of rapid shoaling at $h/h_b = 1.2$ (Fig. 17 (b)), both u' and w' show significant discrepancies between all three models. The curvature of the u' profile between FNBM and 2CLOWNS are similar but the magnitude is larger in FNBM. This could explain why wave breaking occurs earlier in FNBM as the speed of the fluid near the wave crest approaches that of the wave celerity quickly. Although the magnitude of u' is more agreeable between 2CLOWNS and NSWE, the curvature is underestimated implying smaller steepness of the wave shape. Also, w' in NSWE is negative everywhere but it is positive in FNBM everywhere and positive in the lower half of the depth in 2CLOWNS. This is consistent with the apparent small rate of change of the free surface in the NSWE model evident in Fig. 9. The profile of w' is already nonlinear in 2CLOWNS, which NSWE and FNBM cannot assume.

Similarly, in the zone of rapid decay at $h/h_b = 0.96$ (Fig. 17 (c)), the profiles of u' and w' in 2CLOWNS are also highly nonlinear in stark contrast to the linear approximation of w' in NSWE and FNBM. Although the prediction of u' and w' in FNBM at the bottom is in good agreement with 2CLOWNS, they are both underestimated in magnitude at the free surface. This would be expected since at this point rapid decay ($\sim h^4$) occurs in 2CLOWNS but the same degree of decay is not seen for NSWE and FNBM in Fig. 14. The velocity profiles in NSWE are very different to both FNBM and 2CLOWNS. In fact NSWE does not have a region where rapid decay is evident and appears to only mimic gradual decay in Fig. 14. Hence, it is unsurprising that the velocity profiles are not in agreement.

Finally, the velocity profiles in the zone of gradual decay at $h/h_b = 0.70$ where bore propagation has begun to form are plotted in Fig. 17 (d). Notably the profile of u' is extremely irregular in 2CLOWNS. FNBM appears to do a good job in approximating the average magnitude of u' and w' but the velocities particularly at the free surface are significantly different. It is this irregularity of the velocity profiles and the addition of turbulence that makes modelling through traditional wave equations very challenging after wave breaking, even for fairly small wave heights as shown in this example. This is one of the main advantages of using the RANS model in these regions over depth-integrated ones. In addition, although here only solitary wave transformation is demonstrated, such major differences of the vertical velocity profile between RANS, NSWE and FNBM make significant differences in undertow flow for ordinary periodic waves.

8. Concluding remarks

This study introduced a two-way coupled long wave to Reynolds-averaged Navier–Stokes (2CLOWNS) model and applied it to the shoaling and breaking of solitary waves on a plane beach. Firstly, the numerical methods of the individual NSWE and RANS models were introduced followed by a description of the procedure that is utilised to couple the models considering two-way flow. Both disparate spatial and temporal resolutions between the two models were shown to be possible.

Secondly, the shoaling characteristics of the individual NSWE and RANS models were analysed in comparison with expected shoaling rates and a FNBM. The RANS models and FNBM models reproduced gradual and rapid shoaling rates similarly except close to the breaking point. However, comparatively the RANS model is computationally expensive, may suffer from significant numerical dissipation when propagating from offshore, and is sensitive to both horizontal and vertical grid resolution. Conversely, the NSWE model is reliable and efficient in calculating wave propagation from far offshore, however it could not match the steep shoaling rate in the zone of rapid shoaling. By measuring the location where the NSWE model breaks down at the transition into the zone of rapid shoaling, Eq. (30) was derived based on a nondimensional slope parameter to estimate a suitable location to couple NSWE with the RANS model maximising accuracy and efficiency.

A basic evaluation of the 2CLOWNS model was performed to investigate the two-way coupling algorithm and sensitivity to the; 1) assumption of the velocity profile used as a boundary condition to the RANS model during coupling, 2) coupling depth, 3) beach slope and offshore wave height. Incident and reflected waves off a vertical wall could seamlessly pass through the NSWE and RANS domains in both directions using the two-way coupling algorithm on a flat bed with little

sensitivity to the assumption of the velocity boundary conditions. When coupling on a steep slope ($s = 1/20$), during wave shoaling a small hump in the wave height occurs around the coupling interface but the solution recovers a small distance onshore of the interface. The return flow due to the runup and rundown process was able to freely flow out of the RANS domain into the NSWE domain. The sensitivity to the assumption of the vertical velocity profile as a boundary condition to the RANS model was large in comparison to the horizontal velocities. A no gradient condition on both the vertical velocity and the difference in the depth-averaged horizontal velocities was found to give the most robust results for two-way coupling.

If coupling occurs in depths much smaller than that "optimal depth" prescribed by Eq. (30) the NSWE model has diverged too far from the RANS model and accurate wave transformation could not be achieved. The differences between coupling at the optimal depth and a larger one was relatively small but better performance was generally achieved when coupling in larger depths. However, computational time rapidly increases as the coupling depth increases which must be offset against small changes in accuracy. As the slope and offshore wave height increased the relative errors in the form of a deviation in the local wave height at the coupling interface also increased. An equation was derived to describe the deviation in the local wave height as a function of $S_0 s^{-1.095}$. This indicates that the coupling performance is far more sensitive to the offshore wave height in comparison to the slope when coupling at the optimal location. Deviations at the coupling interface are smaller than 1% on any slope, $s<1/20$ with offshore wave height, $A'_0 \leq 0.103$ indicating that reliable results can be achieved in this range. For example, on the slope, $s = 1/60$ with $A'_0 = 0.05$, the 2CLOWNS model could model the entire wave shoaling and breaking process remarkably well in accordance with theoretical expectations and experimental observations. Moreover, the computational time of 2CLOWNS simulations was between 6.2% and 22% that of the computational time using the singular RANS model under the same conditions. In real 2DH/3D large-scale simulations the effect on computational time will be even more dramatic and important.

The ability of 2CLOWNS to predict wave breaking characteristics was analysed and found to give reasonable approximations overall when compared with experimental observations and empirical equations based on results from a FNPF model (Grilli et al., 1997). Eqs. (34) and (35) were derived to determine the water depth at breaking and wave breaking index based on the results of the the 2CLOWNS simulations. The new equations may be a useful complement to the existing ones presented in (Grilli et al., 1997) particularly for $0.10<S_0<0.25$, $S_0/A'_0>1$. Moreover, the post-breaking behaviour and overturning wave shape was presented. The three zones of decay in the local wave height were approximated well overall following estimated rates of decay. Furthermore, the wave shape upon breaking, the formation of the plunging jet, the touchdown of the plunging jet, and wave splashup were all captured in the wave breaking process. Based on plots from FNPF simulations (Grilli et al., 1997) and experimental photographs (Li and Raichlen, 2003) qualitative agreement was found.

Velocity profiles under the wave crest at different locations were compared between NSWE, FNBM and 2CLOWNS simulations for the case $A'_0 = 0.05$ on $s = 1/60$. Good agreement was shown between all three models for both horizontal and vertical velocities near the edge of the zone of gradual shoaling. However, in the zone of rapid shoaling, nonlinear profiles of both u' and w' develop in 2CLOWNS that could not be predicted by NSWE. After breaking, in the zone of gradual decay highly irregular profiles of u' in particular are found in 2CLOWNS which were not possible for NSWE and FNBM to replicate.

Overall it can be concluded that the 2CLOWNS model may prove to be a powerful tool in long wave modelling. This is particularly true for relatively large values of $S_0 s^{-1.095}$ ($A'_0 \leq 0.10$ on mild slopes) as suggested, corresponding to the majority of tsunami situations. For wider applicability to wave problems with larger nonlinearities the use of a higher-order long wave model such as a FNBM instead of a NSWE model to couple to the RANS one should be adopted. Future studies should focus on extending the model and relations presented in this paper in order to apply them robustly to real situations such as computation around offshore and onshore structures of engineering interest. In addition, detailed analysis of the post-breaking physics such as wave splash-up, bore propagation and wave runup will be undertaken in subsequent studies.

Supplementary data to this article can be found online at http://dx.doi.org/10.1016/j.coastaleng.2016.04.011.

Acknowledgements

The authors greatly acknowledge Dr. Patrick Lynett of the University of Southern California for the use of COULWAVE. WP appreciates the continued financial support of the Japanese Ministry of Education, Culture, Sports, Science, and Technology (MEXT).

This research was in part supported by Collaborative Research with DPRI of Kyoto University.

Appendix A. Staggered leap-frog differencing

The staggered leap-frog scheme to solve Eqs. (1) and (2) is described below:

$$\eta_i^{n+1/2} = \eta_i^{n-1/2} + \frac{\Delta t}{\Delta x}\left(Q_{i+1/2}^n - Q_{i-1/2}^n\right) \tag{A.1}$$

$$Q_{i+1/2}^{n+1} = \frac{1}{1+F_x\Delta t}\left[(1-F_x\Delta t)Q_{i+1/2}^n - \Delta t f_{i+1/2} + \frac{\Delta t}{\Delta x} g h_{i+1/2}\left(\psi_{i+1}^{n+1/2} - \psi_i^{n+1/2}\right)\right] \tag{A.2}$$

where $f_{i+1/2}$ is given as:

$$f_{i+1/2} = \frac{gH_{i+1/2}^{n+1/2}}{\Delta x}\left(\eta_{i+1}^{n+1/2} - \eta_i^{n+1/2}\right) + \frac{1}{\Delta x}\left(\lambda_1 \frac{\left(Q_{i-1/2}^n\right)^2}{H_{i-1/2}^n} + \lambda_2 \frac{\left(Q_{i+1/2}^n\right)^2}{H_{i+1/2}^n} + \lambda_3 \frac{\left(Q_{i+3/2}^n\right)^2}{H_{i+3/2}^n}\right) \tag{A.3}$$

and the coefficients of the upwind scheme with truncation error correction are obtained by:

$$\begin{cases} \lambda_1 = -1 + c, & \lambda_2 = 1 - 2c, & \lambda_3 = c, & \text{if } Q_{i+1/2}^n \geq 0, \\ \lambda_1 = -c, & \lambda_2 = -1 + 2c, & \lambda_3 = 1 - c, & \text{if } Q_{i+1/2}^n < 0 \end{cases}$$

where $c = 0.5(1 - Cr)$ is a correction due to the truncation error in the upwind difference. $Cr = \sqrt{gh}\Delta t/\Delta x$ is the local Courant number. This formulation approximates the second-order derivative in the truncation error with a second-order accurate central difference. Because of this the correction is only invoked for computational cells that calculate the implicit dispersion correction ($\frac{\partial \psi}{\partial x} \neq 0$) for stability.

The bottom friction term is given as:

$$F_x = \frac{1}{2}\frac{g n^2 Q_{i+1/2}^n}{\left(H_{i+1/2}^n\right)^{7/3}} \tag{A.4}$$

and total water depths, H at the cell boundaries are calculated by the following:

$$h_{i+1/2} = 0.5(h_{i+1} + h_i)$$
$$H_{i+1/2}^{n+1/2} = 0.5\left(\eta_{i+1}^{n+1/2} + \eta_i^{n+1/2}\right) + h_{i+1/2}$$
$$H_{i+1/2}^{n} = 0.25\left(\eta_{i+1}^{n+1/2} + \eta_i^{n+1/2} + \eta_{i+1}^{n-1/2} + \eta_i^{n-1/2}\right) + h_{i+1/2}$$

where H at the cell boundaries are subject to the condition that they

must be larger than some prescribed value (usually on the order of 1×10^{-3} m) else they are set to 0 and are ignored within the program.

To solve for ψ defined in Eq. (3), the following Poisson-type system of equations is solved:

$$\left(\gamma+\frac{1}{3}\right)\left(\frac{h_i}{\Delta x}\right)^2\left(\psi_{i+1}^{n+1/2}+\psi_{i-1}^{n+1/2}\right)-\left[1+2\left(\gamma+\frac{1}{3}\right)\left(\frac{h_i}{\Delta x}\right)^2\right]\psi_i^{n+1/2} = \left(\gamma+\frac{1}{3}\right)\frac{h_i}{\Delta x}\left(f_{i+1/2}-f_{i-1/2}\right)-\gamma\left(\frac{h_i}{\Delta x}\right)^2\left(\eta_{i-1}^{n+1/2}-2\eta_{i-1}^{n+1/2}+\eta_{i-1}^{n+1/2}\right) \tag{A.5}$$

That is, f is first evaluated using the explicit leapfrog scheme that can be used to obtain the solution to the shallow water equations with $\psi=0$ everywhere. In the case that dispersion is required ψ is calculated through Eq. (A.5) by using a biconjugate gradient stabilized (BiCGSTAB) matrix solver before evaluating Q in Eq. (A.2).

Appendix B. RANS finite differencing and solution method

The finite differencing in the RANS model on the staggered grid (see Fig. 2) and the solution method to Eqs. (4)-(11) is described in this section. A calculation time step begins by obtaining an intermediate velocity field, u^*, w^* from the momentum equations using an explicit first-order Euler time step, that will give the correct vorticity (Tomé et al., 1996) but may not satisfy continuity. Note that the boundary conditions used are the correct ones at the current time step.

$$u_c^* = \overline{u}_c^n-\Delta t\left[g_x+\frac{\overline{p}_e^n-\overline{p}_c^n}{\rho\Delta x}+\Theta_c^n\right] \tag{B.1}$$

where Θ_c^n is given as:

$$\Theta_c^n = -\frac{\overline{u}_c^n}{6\Delta x}\left(2\overline{u}_e^n+3\overline{u}_c^n-6\overline{u}_c^n+\overline{u}_c^n\right)-\frac{\overline{w}_A^n}{6\Delta z}\left(2\overline{u}_{nc}^n+3\overline{u}_c^n-6\overline{u}_{sc}^n+\overline{u}_{Sc}^n\right) +(\nu+\nu_t)\left(\frac{\overline{u}_e^n-2\overline{u}_c^n+\overline{u}_w^n}{(\Delta x^2)}+\frac{\overline{u}_{nc}^n+2\overline{u}_c^n+\overline{u}_{sc}^n}{(\Delta z^2)}\right) \tag{B.2}$$

assuming that $\overline{u}_c^n>0, \overline{w}_A^n=0.25(\overline{w}_c^n+\overline{w}_s^n+\overline{w}_{se}^n+\overline{w}_{ce}^n)>0$. A similar equation can be determined for $\overline{u}_c^n<0, \overline{w}_A^n<0$. The momentum equation in the z-direction to get w^* also follows the same procedure. With u^*, w^* found, the error of continuity is calculated as follows:

$$\frac{\gamma_{xc}^a u_c^*-\gamma_{xw}^a u_w^*}{\Delta x}+\frac{\gamma_{zc}^a w_c^*-\gamma_{zs}^a w_s^*}{\Delta z}=\epsilon_D \tag{B.3}$$

If the maximum absolute value of ϵ_D within the computational region is smaller than some prescribed value usually set to 1×10^{-5}, then u^*, w^* is already divergence free and becomes $\overline{u}^{n+1}$, $\overline{w}^{n+1}$ respectively. Otherwise, the following Poisson pressure equation is solved:

$$\left(\frac{1}{(\Delta x)^2}+\frac{1}{(\Delta z)^2}\right)\psi_c-\frac{1}{(\Delta x)^2}(\psi_e+\psi_w)-\frac{1}{(\Delta z)^2}(\psi_n+\psi_s)\rho\epsilon_D \tag{B.4}$$

The potential function, ψ is then used to update the velocities and pressure:

$$\overline{u}_c^{n+1}=u_c^{*n}-\frac{\psi_e-\psi_c}{\rho\Delta x} \tag{B.5}$$

$$\overline{w}_c^{n+1}=w_c^{*n}-\frac{\psi_n-\psi_c}{\rho\Delta z} \tag{B.6}$$

$$\overline{p}_c^{n+1}=\overline{p}_c^n+\frac{\psi_c}{\Delta t} \tag{B.7}$$

Using the resulting solenoidal velocity field, the F function is updated:

$$F_c^{n+1}=F_c^n-\frac{\Delta t}{\gamma_c^v}\left(\frac{\gamma_{xc}^a(UF)_c-\gamma_{xw}^a(UF)_w}{\Delta x}+\frac{\gamma_{zc}^a(WF)_c-\gamma_{zs}^a(WF)_s}{\Delta z}\right) \tag{B.8}$$

where $(UF)_c$ and $(WF)_c$ are the advected quantities across the cell boundary determined from the PLIC method. The new F fraction is used to define the free surface levels and orientation. Finally, the $k-\varepsilon$ transport equations are solved in a similar fashion to the momentum equations to obtain the new turbulent viscosity, ν_t that is required in Eq. (B.2). Moreover, the above discretizations are shown with uniform Δx, Δz for simplicity, however the model has been coded to consider non-uniform values.

References

Camfield, F.E., Street, R.L., 1969. Shoaling of solitary waves on small slopes. J. Waterw. Harb. Div. 95, 1–22.

Cho, Y.S., Sohn, D.H., Lee, S.O., 2007. Practical modified scheme of linear shallow-water equations for distant propagation of tsunamis. Ocean Eng. 34, 1769–1777. http://dx.doi.org/10.1016/j.oceaneng.2006.08.014.

Fujima, K., 2006. Effect of a submerged bay-mouth breakwater on tsunami behavior analyzed by 2D/3D hybrid model simulation. Nat. Hazards 39, 179–193. http://dx.doi.org/10.1007/s11069-006-0022-x.

Fujima, K., Masamura, K., Goto, C., 2002. Development of the 2D/3D hybrid model for tsunami numerical simulation. Coast. Eng. J. 44, 373–397. http://dx.doi.org/10.1142/S0578563402000615.

Grilli, S.T., Subramanya, R., Svendsen, I.A., Veeramony, J., 1994. Shoaling of solitary waves on plane beaches. J. Waterw. Port Coast. Ocean Eng. 120, 609–628. http://dx.doi.org/10.1061/(ASCE)0733-950X(1994)120:6(609).

Grilli, S.T., Svendsen, I.A., Subramanya, R., 1997. Breaking criterion and characteristics for solitary waves on slopes. J. Waterw. Port Coast. Ocean Eng. 123, 102–112. http://dx.doi.org/10.1061/(ASCE)0733-950X(1997)123:3(102).

Hsiao, S.C., Hsu, T.W., Lin, T.C., Chang, Y.H., 2008. On the evolution and run-up of breaking solitary waves on a mild sloping beach. Coast. Eng. 55, 975–988. http://dx.doi.org/10.1016/j.coastaleng.2008.03.002.

Hwang, K.S., Chang, Y.H., Hwung, H.H., Yi-Syuan, L., 2007. Large scale experiments on evolution and run-up of breaking solitary waves. J. Earthq. Tsunami 1, 257–272. http://dx.doi.org/10.1142/S1793431107000158.

Imamura, F., Yalciner, A.C., Ozyurt, G., 2006. Tsunami Modelling Manual (TUNAMI Model). Technical Report.

Kennedy, A.B., Chen, Q., Kirby, J.T., Dalrymple, R.A., 2000. Boussinesq modeling of wave transformation, breaking, and runup. I: 1D. J. Waterw. Port Coast. Ocean Eng. 126, 39–47. http://dx.doi.org/10.1061/(ASCE)0733-950X(2000)126:1(39).

Kim, D.H., Lynett, P.J., Socolofsky, S.A., 2009. A depth-integrated model for weakly dispersive, turbulent, and rotational fluid flows. Ocean Model. 27, 198–214. http://dx.doi.org/10.1016/j.ocemod.2009.01.005.

Launder, B., Spalding, D., 1974. The numerical computation of turbulent flows. Comput. Methods Appl. Mech. Eng. 3, 269–289. http://dx.doi.org/10.1016/0045-7825(74)90029-2.

Li, Y., Raichlen, F., 2003. Energy balance model for breaking solitary wave runup. J. Waterw. Port Coast. Ocean Eng. 129, 47–59. http://dx.doi.org/10.1061/(ASCE)0733-950X(2003)129:2(47).

Liu, P.L.F., Woo, S.B., Cho, Y.S., 1998. Computer Programs for Tsunami Propagation and Inundation. Technical Report. Cornell University, Ithaca, New York.

Madsen, P.A., Sorensen, O.R., 1992. A new form of the Boussinesq equations with improved linear dispersion characteristics. Part 2. A slowly-varying bathymetry. Coast. Eng. 18, 183–204. http://dx.doi.org/10.1016/0378-3839(92)90019-Q.

Madsen, P.A., Murray, R., Sorensen, O.R., 1991. A new form of the Boussinesq equations with improved linear dispersion characteristics. Coast. Eng. 15, 371–388. http://dx.doi.org/10.1016/0378-3839(91)90017-B.

McCowan, J., 1891. On the solitary wave. Philos. Mag. Ser. 5 32, 45–58. http://dx.doi.org/10.1080/14786449108621390.

Munk, W.H., 1949. The solitary wave theory and its application to surf problems. Ann. N. Y. Acad. Sci. 51, 376–424. http://dx.doi.org/10.1111/j.1749-6632.1949.tb27281.x.

Nwogu, O., 1993. Alternative form of Boussinesq equations for nearshore wave propagation. J. Waterw. Port Coast. Ocean Eng. 119, 618–638. http://dx.doi.org/10.1061/(ASCE)0733-950X(1993)119:6(618).

Pringle, W.J., Yoneyama, N., 2013. The Application of a Hybrid 2D/3D Numerical Tsunami Inundation-Propagation Flow Model to the 2011 off the Pacific Coast of Tohoku Earthquake Tsunami. J. Jpn. Soc. Civ. Eng. Ser. B2 Coast. Eng. 69, I_306–I_310 (in Japanese. doi: 10.2208/kaigan.69.I_306).

Pringle, W.J., Yoneyama, N., 2014. Solitary wave runup on a plane beach using a two-way coupled depth-averaged shallow water - RANS VOF model. 19th IAHR-APD Congress, Hanoi, Vietnam, p. 8.

Roeber, V., Cheung, K.F., 2012. Boussinesq-type model for energetic breaking waves in fringing reef environments. Coast. Eng. 70, 1–20. http://dx.doi.org/10.1016/j.coastaleng.2012.06.001.

Schember, H.R., 1982. A new model for three-dimensional nonlinear dispersive long waves Ph.D. thesis California Institute of Technology (URL: http://thesis.library.caltech.edu/3729/1/Schember_HR_1982.pdf).

Shi, F., Kirby, J.T., Harris, J.C., Geiman, J.D., Grilli, S.T., 2012. A high-order adaptive time-stepping TVD solver for Boussinesq modeling of breaking waves and coastal inundation. Ocean Model. 43, 36–51. http://dx.doi.org/10.1016/j.ocemod.2011.12.004.

Shigihara, Y., Fujima, K., 2007. Adequate numerical scheme for dispersive wave theory for tsunami simulation and development of new numerical algorithm. Doboku Gakkai Ronbunshu B/JSCE. J. Hydraul. Coast. Environ. Eng. 63, 51–66. http://dx.doi.org/10.2208/jscejb.63.51.

Shuto, N., 1991. Numerical simulation of tsunamis - its present and near future. Nat. Hazards 4, 171–191. http://dx.doi.org/10.1007/BF00162786.

Sitanggang, K.I., Lynett, P.J., 2010. Multi-scale simulation with a hybrid Boussinesq-RANS hydrodynamic model. Int. J. Numer. Methods Fluids 62, 1013–1046. http://dx.doi.org/10.1002/fld.2056.

Son, S., Lynett, P.J., Kim, D.H., 2011. Nested and multi-physics modeling of tsunami evolution from generation to inundation. Ocean Model. 38, 96–113. http://dx.doi.org/10.1016/j.ocemod.2011.02.007.

Synolakis, C.E., 1986. The runup of long waves Ph.D. thesis California Institute of Technology (URL: http://thesis.library.caltech.edu/3506/1/Synolakis_ce_1986.pdf).

Synolakis, C.E., 1987. The runup of solitary waves. J. Fluid Mech. 185, 523–545. http://dx.doi.org/10.1017/S002211208700329X.

Synolakis, C.E., Skjelbreia, J.E., 1993. Evolution of maximum amplitude of solitary waves on plane beaches. J. Waterw. Port Coast. Ocean Eng. 119, 323–342. http://dx.doi.org/10.1061/(ASCE)0733-950X(1993)119:3(323).

Synolakis, C.E., Bernard, E.N., Titov, V.V., Kanoglu, U., González, F.I., 2009. Validation and verification of tsunami numerical models. Pure Appl. Geophys. 165, 2197–2228. http://dx.doi.org/10.1007/s00024-004-0427-y.

Titov, V.V., Synolakis, C.E., 1995. Modeling of breaking and nonbreaking long-wave evolution and runup using VTCS-2. J. Waterw. Port Coast. Ocean Eng. 121, 308–316. http://dx.doi.org/10.1061/(ASCE)0733-950X(1995)121:6(308).

Tomé, M.F., Duffy, B., McKee, S., 1996. A numerical technique for solving unsteady non-Newtonian free surface flows. J. Non-Newtonian Fluid Mech. 62, 9–34. http://dx.doi.org/10.1016/0377-0257(95)01391-1.

Tonelli, M., Petti, M., 2009. Hybrid finite volume-finite difference scheme for 2DH improved Boussinesq equations. Coast. Eng. 56, 609–620. http://dx.doi.org/10.1016/j.coastaleng.2009.01.001.

Wei, G., Kirby, J.T., 1995. Time-dependent numerical code for extended Boussinesq equations. J. Waterw. Port Coast. Ocean Eng. 121, 251–261. http://dx.doi.org/10.1061/(ASCE)0733-950X(1995)121:5(251).

Wei, G., Kirby, J.T., Grilli, S.T., Subramanya, R., 1995. A fully nonlinear Boussinesq model for surface waves. Part 1. Highly nonlinear unsteady waves. J. Fluid Mech. 294, 71–92. http://dx.doi.org/10.1017/S0022112095002813.

Yoneyama, N., Matsuyama, M., Tanaka, H., 2002. Numerical analysis for locally high runup of the 1993 Hokkaido Nansei-oki tsunami. J. Hydraul. Coast. Environ. Eng. JSCE 705, 139–150 (in Japanese. doi: 10.2208/jscej.2002.705_139).

Youngs, D., 1982. Time-Dependent Multi-Material Flow with Large Fluid Distortion. In: Morton, K.W., Baines, M.J. (Eds.), Numerical Methods for Fluid Dynamics Vol. 24. Academic Press, pp. 273–285.